Probabilistic Assessment of Antarctic Thermomechanical Structure: Impacts on Ice Sheet Stability

James A. N. Hazzard*[1], Fred D. Richards[1], Saskia D. B. Goes[1], Gareth G. Roberts[1]

1. Department of Earth Science & Engineering, Imperial College London, Royal School of Mines, Prince Consort Road, London, SW7 2AZ, UK

*j.hazzard20@imperial.ac.uk

Key Points:

1. Bayesian inversion procedure is used to calibrate experimental parameterisations of anelasticity, allowing the conversion of upper mantle shear wave velocities directly into temperature, density and viscosity structure
2. Probabilistic approach enables reliable uncertainty quantification of raw thermomechanical outputs as well as lithosphere-asthenosphere boundary (LAB) depth and geothermal heat flow (GHF)
3. Evidence for significant lateral heterogeneity in Antarctic mantle viscosity (10^{19} to 10^{23} Pa s), LAB depth (40 to 350 km) and GHF (40 to 100 mW m^{-2}) is obtained, corroborated by data from the geological record

Abstract

Uncertainty in present-day glacial isostatic adjustment (GIA) rates represent at least 44% of the total gravity-based ice mass balance signal over Antarctica. Meanwhile, physical couplings between solid Earth, sea level and ice dynamics enhance the dependency of the spatiotemporally varying GIA signal on three-dimensional variations in mantle rheology. Improved knowledge of thermomechanical mantle structure is therefore required to refine estimates of current and projected ice mass balance. Here, we present a Bayesian inverse method for self-consistently mapping shear-wave velocities from high-resolution adjoint tomography into thermomechanical structure using calibrated parameterisations of anelasticity at seismic frequency. We constrain the model using regional geophysical data sets containing information on upper mantle temperature, attenuation and viscosity structure. Our treatment allows formal quantification of parameter covariances, and naturally permits propagation of material parameter uncertainties into thermomechanical structure estimates. We find that uncertainty in steady-state viscosity structure at 150 km depth can be reduced by 4–5 orders of magnitude compared with a forward-modelling approach neglecting covariance. By accounting for the dependence of viscosity on loading timescale, we find good agreement between our estimates of mantle viscosity beneath the Amundsen Sea Embayment, and those derived from satellite GPS. Direct access to temperature structure allows us to estimate lateral variations in lithosphere-asthenosphere boundary (LAB) depth, geothermal heat flow (GHF), and associated uncertainties. We find evidence for shallow LAB depths (60 ± 10 km), and high GHF (72 ± 6 mW m^{-2}) beneath West Antarctica, suggesting a highly dynamic response to ice mass loss.

Plain Language Summary

The viscosity (i.e., "runniness") and temperature of Earth's interior exert a major influence on ice sheet stability and sea level change. Viscosity structure controls how the shape of Earth's surface and gravity field distorts when ice melts. Temperature structure controls the flow of heat to the base of ice sheets, determining how rapidly they slide and deform. Both parameters are expected to vary significantly with position inside Earth's mantle, but are poorly constrained. Improved information about mantle structure can be derived from recent models telling us about spatial variations in the speed at which earthquake-generated waves travel through Earth. In this study, we present a statistical method allowing us to convert from such models into estimates of viscosity and temperature. This method enables us to reduce uncertainty on viscosity structure by 4–5 orders

of magnitude, compared to a typical approach. Our estimates of viscosity beneath the Amundsen Sea Embayment are in close agreement with observations from satellite GPS. In addition, our models of temperature structure allow us to estimate variations in Antarctic tectonic plate thickness, geothermal heat flow, and their associated uncertainties. We find evidence for significant disparity in each of these structures between West and East Antarctica.

---

1 Introduction

Antarctica is host to a volume of ice equivalent to 57.9 ± 0.9 m of global mean sea level (GMSL) rise, or roughly 90% of the global cryosphere (Bamber et al., 2018; Morlighem et al., 2020). The mantle structure, topography, and glacial stability of this continent expresses a dichotomy in tectonic setting between East and West Antarctica. The two regions are separated by the Transantarctic Mountain Range, which spans the continental interior from the Weddell Sea to the Ross Sea. As a result, Antarctica's grounded ice volume is divided into an East and West Antarctic Ice Sheet (EAIS and WAIS, respectively). The EAIS is underlain by thick, cratonic lithosphere owing to minimal tectonic activity in this region since the Mesozoic Era (Noble et al., 2020). The WAIS is underlain by an active rift system, which has given rise to upwelling of low viscosity asthenosphere, and dynamically thinned lithosphere (Noble et al., 2020). Bedrock elevation is predominantly above GMSL in the east, and below GMSL in the west (Figure 1a). This exerts a major influence on ice dynamics, due to the increased vulnerability of marine-grounded ice, especially when positioned on a reverse bed slope, as is the case in West Antarctica (Fretwell et al., 2013). The WAIS is therefore considered much more prone to short-term ice mass loss (Coulon et al., 2021). Indeed, it is declining by $\sim$ 200 Gt per year, while it is unknown whether the EAIS is gaining or losing mass (Shepherd et al., 2018).

To predict the contribution of the AIS to future patterns of spatiotemporally variable sea level, we require a reliable assessment of its stability. This involves detailed insight on past ice volumes from the geological record (DeConto et al., 2016), quantification of present-day ice mass balance (Caron et al., 2018), and physically accurate models for the future evolution of the cryosphere (Slangen et al., 2017). A vital consideration in each of these pursuits is solid Earth structure and dynamics. Time-dependent lithospheric deflections caused by evolving surface loads and mantle flow alter the elevation of palaeo sea level indicators, the shape of the oceans and gravity field, and the stability of grounded ice (Austermann et al., 2015; Gomez et al., 2018; Mitrovica et al., 2020). These coupled interactions between solid Earth, ocean and cryosphere operate on physical time scales ranging from decadal to geological, and depend heavily on upper mantle thermomechanical structure.

For example, contemporary estimates of ice mass balance typically rely on satellite missions recording either altimetric or gravimetric data (Zwally et al., 2011; Shepherd et al., 2018, 2020). The Gravity Recovery and Climate Experiment (GRACE) and its successor GRACE Follow-On (GRACE-FO) offer indirect regional scale insight into ice mass balance via the tracking of temporal changes in Earth's gravity field (King et al., 2012). However, glacial isostatic adjustment (GIA; the viscoelastic response of the solid Earth to changes in the distribution of ice and water over its surface) influences the gravity field significantly, even on decadal timescales. Since the Earth is still

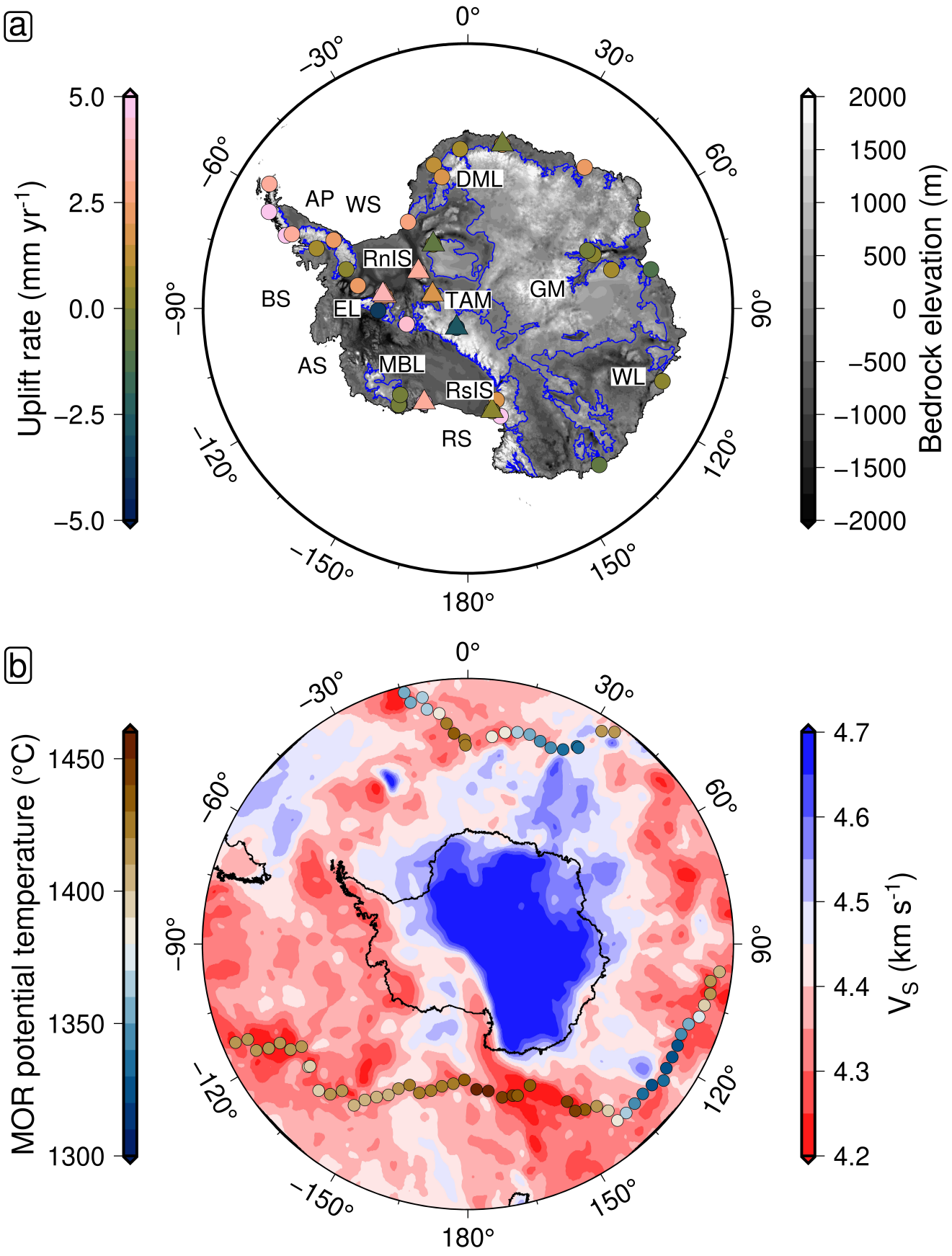

Figure 1: **Geophysical and geochemical constraints on Antarctic mantle dynamics and structure.** (a) Antarctic bedrock elevation taken from BEDMAP2 data (Fretwell et al., 2013), with elastically corrected GPS uplift rate overlain (Thomas et al., 2011, circles: individual measurement sites; triangles: averages over local sites). Blue contours delineate the transition between positive and negative bedrock elevation. Regions of negative elevation around the periphery of the continent indicate where the AIS is marine-grounded. Text labels indicate reference points within Antarctica and the surrounding ocean (AP: Antarctic Peninsula; RnIS: Ronne Ice Shelf; WS: Weddell Sea; DML: Dronning Maud Land; GM: Gamburtsev Mountain Range; WL: Wilkes Land; RS: Ross Sea; RsIS: Ross Ice Shelf; MBL: Marie Byrd Land; TAM: Transantarctic Mountain Range; AS: Amundsen Sea; EL: Ellsworth Land; BS: Bellingshausen Sea). (b) V_S at 150 km depth from ANT-20 tomographic model (Lloyd et al., 2020), with mid-ocean ridge (MOR) potential temperature overlain (Dalton et al., 2014).

responding today to deglaciation following the Last Glacial Maximum (LGM; 21 ka), with elastically adjusted GPS uplift rates ranging from -5 to 5 mm a^{-1} across Antarctica (Thomas et al., 2011; Figure 1a), this contaminating GIA signal must be removed to accurately determine contemporary ice mass balance. However, calculation of the GIA signal relies upon two main inputs that remain weakly constrained; the first being a reconstruction of ice sheet history, and the second a viscoelastic Earth model. Caron et al. (2018) estimated that the Antarctic GIA uncertainty was around 44% of the total amplitude of the GRACE gravity signal itself. The true uncertainty is likely to be even larger, since the aforementioned study does not account for significant lateral heterogeneities in upper mantle viscosity inferred from GPS observations across Antarctica (Barletta et al., 2018). The quality of projections of future sea level change is also heavily reliant on our ability to model GIA as accurately and precisely as possible. GIA models that incorporate solid Earth feedbacks will be particularly sensitive to the underlying mantle rheology, since this acts as a direct control on the evolution of the ice sheet (Whitehouse, 2018). For example, the presence of low-viscosity mantle beneath melting marine-based ice sheet sectors such as the Amundsen Sea Embayment may delay or even prevent unstable grounding line retreat (Barletta et al., 2013). This enhanced dependence of sea level projections on our knowledge about mantle viscosity and temperature structure points to the requirement for coupled ice sheet-sea level modelling, incorporating reliable estimates of 3-D mantle structure (Gomez et al., 2018).

Seismic shear-wave velocity (V_S) can be used to gain insight into upper mantle structure beneath the ice sheets due to its strong sensitivity to temperature (Faul et al., 2005). Laboratory experiments show sub-solidus temperature changes can induce up to 20% variations in V_S (Priestley et al., 2013; and references therein). Although volatiles and composition may also influence V_S (Karato et al., 1998; Lee, 2003), recent studies show close agreement between xenolith-derived temperature profiles and those inferred from seismic tomography models using anelastic parameterisations that ignore the potential impact of compositional heterogeneity in the asthenosphere and lower lithosphere, indicating that temperature is indeed the dominant control on shallow mantle V_S variation (Hoggard et al., 2020; Klöcking et al., 2020).

Until recently, Antarctica has suffered from a significant shortage of seismic data due in part to difficulties operating polar seismic stations and the lack of proximal (latitudinally) land masses (Lloyd et al., 2020). However, ANT-20, a wave-equation traveltime adjoint tomography model, has recently been developed utilising data from 323 seismic stations, the majority (297) of which reside on the Antarctic continent (Lloyd et al., 2020). ANT-20 is the first continental model to image Antarctica at regional-scale resolution ($\sim$ 100 km), and thus serves as a suitable starting point for mapping temperature and viscosity with unprecedented fidelity. Promisingly, this tomographic model contains many features that are consistent with independent constraints. For example, lateral variations in V_S beneath the Antarctic mid-ocean ridge system correlate well with point estimates of potential temperature (Dalton et al., 2014; Figure 1b). Fast shear-wave velocities below East Antarctica are indicative of high viscosity lithosphere and slow velocities in the West point to low viscosities and thus short viscoelastic response timescales (Coulon et al., 2021).

Here we present a novel Bayesian inverse framework for self-consistent quantification of upper mantle thermo-mechanical structure from seismic data via the calibration of experimental parameterisations of anelasticity. To

achieve this, the deterministic approach set out by Richards et al. (2020b) is recast in terms of statistical methods. First, the details of the modelling approach are discussed, as well as the geophysical data used to constrain the inversion, and its algorithmic implementation. Second, the inversion is applied to the ANT-20 model of Antarctic shear-wave velocity structure and trade-offs between anelasticity parameters are quantified. Third, seismologically derived estimates of viscosity, temperature, lithosphere-asthenosphere boundary (LAB) depth and geothermal heat flow (GHF) are presented. For the first time, uncertainties in each of these outputs are constrained using stochastic methods. Finally, the physical outputs presented herein are evaluated in the context of other studies, and potential implications and remaining challenges are discussed. Our principal goal is to show how disparate geophysical constraints can be integrated within a probabilistic inverse framework to develop a quantitative understanding of Antarctic upper mantle thermomechanical structure and its associated uncertainties.

2 Converting seismic velocities into thermomechanical parameters

In order to use V_S data to gain insight into upper mantle structure, a physical model must be employed. Most studies have taken an empirical approach to converting between V_S and viscosity, making use of a constant or depth-dependent scaling (e.g. Austermann et al., 2013; Milne et al., 2018; Davies et al., 2019; Steinberger et al., 2019). Such conversions fail to appropriately capture non-linear viscosity reductions observed near the solidus in laboratory experiments (Faul et al., 2007; McCarthy et al., 2011; Takei, 2017; Yabe et al., 2020).

To better account for observed non-linearities, we use the anelastic parameterisation of Yamauchi et al. (2016), hereafter YT16. YT16 incorporates the effect of pre-melting, a process which enhances diffusionally accommodated grain boundary sliding and high-frequency seismic attenuation. By doing so, the model provides a physical basis for significant non-linearity in the $V_S(T)$ relationship near and beyond the solidus temperature (homologous temperature, $T/T_S \sim 1$). Since YT16 made use of a polycrystal analogue of the olivine-basalt system with a much smaller melting temperature, their forced oscillation experiments conducted near room temperature can tap into the same normalised frequency range as seismic waves at the near-solidus conditions relevant to the upper mantle.

YT16 make use of the complex compliance $J^*(\omega) = J_1(\omega) + iJ_2(\omega)$ in their description of anelasticity, which relates the complex strain response $\varepsilon^*(t)$ of a linear viscoelastic material to an applied complex stress $\sigma^*(t)$.

$$\sigma^*(t) = \int \sigma_0 \exp(-i\omega t)\,\mathrm{d}\omega, \tag{1}$$

$$\varepsilon^*(t) = \int J^*(\omega)\sigma_0 \exp(-i\omega t)\,\mathrm{d}\omega. \tag{2}$$

The in-phase term of the complex compliance J_1 is known as the storage compliance, as it is energy conserving. The out-of-phase term J_2 is known as the loss compliance, as it is responsible for dissipation. This relationship can be verified by considering the work done by the system during a complete oscillation cycle (Appendix A).

Consider a plane wave propagating in a linear viscoelastic medium, as an approximation of seismic wave propagation in the mantle. The dependence of the phase velocity $V(\omega)$ and attenuation $Q^{-1}(\omega)$ on the complex

compliance is given by

$$V = \frac{1}{\sqrt{\rho J_1}}, \tag{3}$$

$$Q^{-1} = \frac{J_2}{J_1}, \tag{4}$$

where ρ is the density of the medium (McCarthy et al., 2011). These equations hold for seismological studies of the mantle, where the approximation $Q^{-1} \ll 1$ is valid (Takei, 2017). The complex compliance terms can be determined given knowledge of temperature, pressure, seismic frequency, and a set of anelastic parameters. This allows conversion from temperature to V_S, as well as vice versa given some optimisation procedure.

Of the various parameters involved in YT16, seven are material properties that depend upon the makeup of the mantle. Hereafter, this group of seven parameters are referred to as the model space. The first three parameters regulate the elastic component of the material response, namely the unrelaxed shear modulus at reference temperature and pressure, μ_0, and the temperature and pressure derivatives of the shear modulus, $\partial\mu/\partial T$ and $\partial\mu/\partial P$, respectively. The last four parameters control the transient component of the response, namely reference viscosity, η_0, activation energy, E_A, activation volume, V_A and the depth gradient of the solidus temperature, $\partial T_S/\partial z$.

A forward-modelling approach is commonly used to account for anelasticity in the conversion of V_S into thermomechanical parameters (Cammarano et al., 2003). The elastic component of $V_S(P,T)$ is modelled by combining an assumed mantle composition with a computational Gibbs free energy minimisation to estimate μ_0, $\partial\mu/\partial T$ and $\partial\mu/\partial P$. A correction for anelastic behaviour is then applied using values of η_0, E_A, V_A and $\partial T_S/\partial z$ compiled from laboratory-based experiments on mantle minerals. There are two key drawbacks to this method. The first is that applying experimentally determined parameter values to mantle conditions requires extrapolation of grain size-dependent behaviour across several orders of magnitude, the validity of which remains unclear. The second is that discrepancies between tomography models are introduced by subjective choices such as regularisation, model parameterisation, and choice of reference model (Richards et al., 2020b). The forward approach then becomes problematic as, for a constant choice of anelasticity parameters, highly discrepant physical predictions are generated depending on the chosen velocity model.

To tackle these issues and ensure a conversion consistent with Antarctic geophysical data, we instead calibrate the seven-dimensional YT16 model space against a suite of regional temperature, attenuation and viscosity constraints (Priestley et al., 2006, 2013; Richards et al., 2020b). Note that the framework presented in this study is applicable to any choice of anelastic parameterisation. Calibration is achieved within the framework of a Bayesian inversion, incorporating stochastic sampling to characterise the model space. These samples can then be used to propagate uncertainties in the anelastic model to formal uncertainties in the resulting rheological model.

2.1 Independent geophysical data sets

Independent constraints on mantle properties are collated and used as data sets in a joint inversion. These data are complementary in that they are collected over a range of depths (0 to 400 km) and temperatures (0 to 1500 °C), and help to tackle the issue of non-uniqueness via their different sensitivities to a given change in the parameter

space.

The first constraint used is the observed $V_S(T)$ relationship in conductively cooling oceanic lithosphere. V_S data from a tomographic model may be compared to thermal structure obtained via numerical modelling when binned by age and depth (Richards et al., 2020b). The 15 km maximum vertical resolution of ANT-20 informs our decision to sample V_S and T data points in 25 km bins over the range 50 to 125 km. This depth range is chosen to avoid non-negligible compositional effects at shallow depths due to mantle melting and the potential incorporation of spurious low velocity structure resulting from the bleeding of crustal velocities down into deeper depth ranges.

To construct a suitable thermal model for Antarctica, a Crank-Nicholson finite difference scheme with a predictor-corrector step is used to numerically integrate the heat diffusion equation. We follow the implementation set out by Richards et al. (2018) and Richards et al. (2020a), in which the heat capacity, C_P, mantle density, ρ, and thermal conductivity, k, vary as a function of temperature, T, and composition, X. The latter two variables are also dependent on pressure, P.

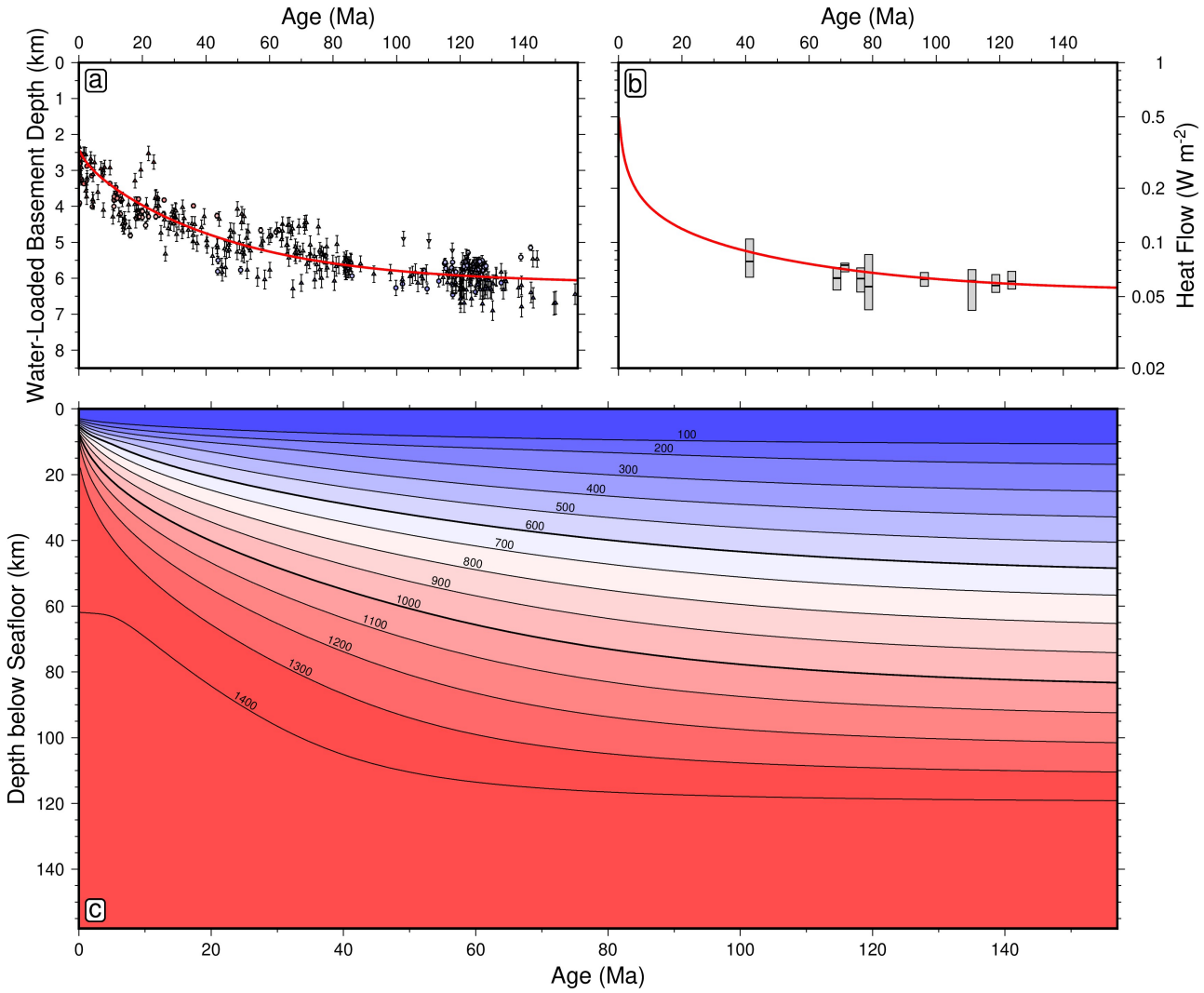

Figure 2: **Thermal modelling of Antarctic oceanic lithosphere.** (a) Thermal model fit to oceanic age-depth data from the Antarctic oceanic region placed into 2.5 Ma bins (Richards et al., 2018). (b) Same as (a) for age-heat flow data (Richards et al., 2018). (c) Plate cooling model solution constructed using a Crank-Nicholson finite-difference scheme to numerically solve the 1-D heat-diffusion equation (Richards et al., 2018; Richards et al., 2020a). Antarctica-specific regional data are used to capture any local deviation from the globally averaged thermal trend. Model isotherms (°C) given by black curves in panel (c).

Mantle potential temperature, plate thickness and zero-age ridge depth are optimised by assessing the misfit to heat flux and subsidence data located within the footprint of the ANT-20 seismic tomographic model. The result is a best-fitting model describing the thermal structure beneath the oceans surrounding Antarctica (see Figure 2), suitable for comparison with V_S measurements over the same age-depth bins, such that the regional oceanic $V_S(T)$ relationship can be obtained for the lithosphere. We find a mantle potential temperature of $T_P = 1420 \pm 50$ °C, approximately 5% hotter than the geochemically constrained global average $T_P = 1333$ °C (Richards et al., 2018). In the inversion, V_S measurements are compared to inferences of V_S from temperature at each age-depth bin (Figure 4a).

Since the lithospheric thermal model is only applicable at depths of $z \leq 125$ km, a $T_P = 1420$ °C (1693 K) isentrope is used to characterise temperatures in the convective portion of the mantle, over the depth range $z = 225$ to 400 km. Here, temperature is calculated according to

$$T = T_P \exp\left(\frac{\alpha g z}{C_P}\right), \tag{5}$$

where α is thermal expansivity, g, acceleration due to gravity, and z, depth. This serves as the second constraint in the inversion, whereby V_S measurements are compared to inferences of V_S from temperature at each depth bin (Figure 4b). The third constraint is the QRFSI12 attenuation model of Dalton et al. (2014), which provides an average radial profile of seismic attenuation at depths $z = 150$ to 400 km beneath Antarctic ocean floor of age ≥ 100 Ma. Both the isentropic temperature and attenuation profiles are sampled at 25 km intervals to match the chosen V_S binning resolution (Figure 4c). To assess the misfit between data and model for these two constraints, tomographic V_S measurements are compared to V_S inferred from isentropic temperature, and attenuation measurements are compared to attenuation inferred from tomographic V_S, respectively. The final constraint used is a single estimate for the average steady state shear viscosity between 225 to 400 km depth, $\eta = 10^{20\pm1}$ Pa s (Lau et al., 2016, based on GIA modelling of relative sea-level and geodetic data assuming a Maxwell rheology, i.e. diffusion creep). Here, the viscosity constraint is compared to the corresponding depth-averaged viscosity inferred from V_S (Figure 4d).

2.2 Bayesian modelling framework

Formulating the inverse problem in a Bayesian framework entails treating each of the model parameters as random variables. There are several reasons why this is favourable to taking a deterministic approach. By incorporating hyperparameters, the reported uncertainties on each data set are scaled to more appropriately capture the misfit between data and model (see Eilon et al., 2018). This approach allows for integration of multiple constraints into a joint inversion without the need to use subjective weightings on each data set (Fukuda et al., 2010). Secondly, prior information on the nature of the parameter space can be incorporated. Thirdly, the use of statistical sampling enables much more informative and rigorous treatment of uncertainty, and a natural way to propagate this into uncertainty in physical parameters of interest.

The objective of the inversion is to numerically characterise the *a posteriori* probability density function $p(\boldsymbol{\mathcal{X}}|\boldsymbol{\mathcal{D}})$. This function describes how the probability of an infinitesimal volume, $d\boldsymbol{\mathcal{X}}$, of the model space, $\boldsymbol{\mathcal{X}}$, varies as we

traverse through it. In the following, we will refer to a particular choice of model using the superscript notation, $\boldsymbol{\mathcal{X}}^i$. We will refer to a particular component of the model using the subscript notation, $\mathcal{X}_i$.

The model space $\boldsymbol{\mathcal{X}} = \boldsymbol{\mathcal{X}}(\boldsymbol{m}, \boldsymbol{\sigma})$ contains seven anelastic model parameters

$$\boldsymbol{m} = \left[\mu_0, \partial\mu/\partial T, \partial\mu/\partial P, \eta_0, E_A, V_A, \partial T_S/\partial z\right]^T, \tag{6}$$

as well as three hyperparameters

$$\boldsymbol{\sigma} = \left[\sigma_1, \sigma_2, \sigma_3\right]^T. \tag{7}$$

An individual hyperparameter is used to tune the uncertainties for each data set. We omit a fourth hyperparameter associated with the viscosity constraint, due to the instability of this parameter when used to constrain a data set containing only a single data point. The posterior density, $p(\boldsymbol{\mathcal{X}}|\boldsymbol{\mathcal{D}})$, is dependent on the outcome of the experiments we undertake, via our data, $\boldsymbol{\mathcal{D}}$. Since it is usually not possible to access $p(\boldsymbol{\mathcal{X}}|\boldsymbol{\mathcal{D}})$ analytically, we turn to stochastic methods.

Bayes' theorem states that the *a posteriori* density, $p(\boldsymbol{\mathcal{X}}|\boldsymbol{\mathcal{D}})$, is linked to the *a priori* information we have about the model space, as well as the likelihood of obtaining the observed data given a particular model, which are described by the density functions, $p(\boldsymbol{\mathcal{X}})$ and $p(\boldsymbol{\mathcal{D}}|\boldsymbol{\mathcal{X}})$, respectively. The relationship is expressed mathematically as

$$p(\boldsymbol{\mathcal{X}}|\boldsymbol{\mathcal{D}}) = \frac{p(\boldsymbol{\mathcal{X}})p(\boldsymbol{\mathcal{D}}|\boldsymbol{\mathcal{X}})}{p(\boldsymbol{\mathcal{D}})}. \tag{8}$$

The *a priori* probability density on the data, $p(\boldsymbol{\mathcal{D}})$, takes on a fixed value for a given set of observations and is thus treated as a normalisation. This allows us to compare probability densities between two different models $\boldsymbol{\mathcal{X}}^1$ and $\boldsymbol{\mathcal{X}}^2$ by evaluating the ratio

$$\frac{p(\boldsymbol{\mathcal{X}} = \boldsymbol{\mathcal{X}}^1|\boldsymbol{\mathcal{D}})}{p(\boldsymbol{\mathcal{X}} = \boldsymbol{\mathcal{X}}^2|\boldsymbol{\mathcal{D}})} = \frac{p(\boldsymbol{\mathcal{X}} = \boldsymbol{\mathcal{X}}^1)p(\boldsymbol{\mathcal{D}}|\boldsymbol{\mathcal{X}} = \boldsymbol{\mathcal{X}}^1)}{p(\boldsymbol{\mathcal{X}} = \boldsymbol{\mathcal{X}}^2)p(\boldsymbol{\mathcal{D}}|\boldsymbol{\mathcal{X}} = \boldsymbol{\mathcal{X}}^2)}. \tag{9}$$

Therefore, to estimate the variation in posterior density one needs a suitable method for calculating the prior and likelihood functions. The prior should be selected as a function which agnostically summarises the knowledge one has about the model space before performing the inversion, usually in the form of a uniform or Gaussian distribution. Here we use a Gaussian distribution to summarise our prior knowledge of each parameter $\mathcal{X}_i$,

$$p(\mathcal{X}_i) = \frac{1}{\sqrt{2\pi}s_i} \exp\left(-\frac{(\mathcal{X}_i - \mu_i)^2}{2s_i^2}\right), \tag{10}$$

where μ_i and s_i represent our prior estimate and its uncertainty respectively. This distribution is useful as it enforces a non-zero probability density for any choice of model, $\boldsymbol{\mathcal{X}}^i$, and enables us to use conservative uncertainty estimates for model parameters based on experimental studies (Table 1). The assumption that each model parameter is conditionally independent is taken, allowing the multiplication of the prior on each parameter to form an overall

Model sector	Model parameter i	Prior μ_i	Prior s_i	Posterior μ_i	Posterior s_i	MAP
Anelasticity parameters $\boldsymbol{m}$	μ_0 [GPa]	81	8	74.8	0.4	74.8
	$\partial\mu/\partial T$ [GPa K^{-1}]	-0.014	0.003	-0.0129	0.0046	-0.0131
	$\partial\mu/\partial P$ [unitless]	1.6	0.2	2.04	0.06	2.09
	$\log_{10}\left(\eta_0[\text{Pa s}]\right)$	22	3	23.2	0.7	22.9
	E_A [kJ mol^{-1}]	400	200	542	146	476
	V_A [cm^3 mol^{-1}]	6	4	5.35	0.32	5.02
	$\partial T_S/\partial z$ [K km^{-1}]	2.25	2.25	1.63	0.14	1.65
Hyperparameters $\boldsymbol{\sigma}$	$\log_{10}\left(\sigma_1\ [\text{unitless}]\right)$	0	1	-0.317	0.024	-0.328
	$\log_{10}\left(\sigma_2\ [\text{unitless}]\right)$	0	1	0.093	0.148	0.136
	$\log_{10}\left(\sigma_3\ [\text{unitless}]\right)$	0	1	0.588	0.105	0.514

Table 1: Prior and posterior estimates of the seven material-dependent components of YT16, denoted by $\boldsymbol{m}$, as well as the three hyperparameters, denoted by $\boldsymbol{\sigma}$. Prior μ_i and s_i represent the mean and standard deviation of the Gaussian prior distribution for each parameter. For details of prior calculation, see Appendix B. Posterior μ_i and s_i are estimates of the mean and standard deviation of the posterior distribution for each parameter. MAP represents the maximum *a posteriori* model.

prior density given by

$$p(\boldsymbol{\mathcal{X}}) = \prod_{i=1}^{i=N_\text{p}} \frac{1}{\sqrt{2\pi}s_i} \exp\left(-\frac{(\mathcal{X}_i - \mu_i)^2}{2s_i^2}\right), \tag{11}$$

where N_p is the number of parameters within the model.

We will also assume that the data points within each data set are independent, allowing us to use a Gaussian distribution to describe the likelihood function for each data set,

$$p(\boldsymbol{d}_k|\boldsymbol{\mathcal{X}}(\boldsymbol{m},\boldsymbol{\sigma})) = \frac{1}{(2\pi\sigma_k^2)^{N_\text{k}/2}|\boldsymbol{\Sigma_k}|^{1/2}} \exp\left(-\frac{1}{2\sigma_k^2}\left(\boldsymbol{d}_k - \hat{\boldsymbol{d}}_k\right)^T \boldsymbol{\Sigma}_\boldsymbol{k}^{-1}\left(\boldsymbol{d}_k - \hat{\boldsymbol{d}}_k\right)\right). \tag{12}$$

In this equation, $\boldsymbol{d}_k$ represents the k^{th} data set containing N_k data points, $\hat{\boldsymbol{d}}_k = \hat{\boldsymbol{d}}_k(\boldsymbol{\mathcal{X}})$ the corresponding model prediction, $\boldsymbol{\Sigma_k}$ the data covariance matrix containing the uncertainty on each data point, and σ_k the hyperparameter weighting applied to the data set.

If the data sets are independent of each other, the overall likelihood function can be constructed by simply multiplying together the likelihood function for each of the N_d data sets:

$$p(\boldsymbol{\mathcal{D}}|\boldsymbol{\mathcal{X}}(\boldsymbol{m},\boldsymbol{\sigma})) = \prod_{k=1}^{k=N_\text{d}} \frac{1}{(2\pi\sigma_k^2)^{N_\text{k}/2}|\boldsymbol{\Sigma_k}|^{1/2}} \exp\left(-\frac{1}{2\sigma_k^2}\left(\boldsymbol{d}_k - \hat{\boldsymbol{d}}_k\right)^T \boldsymbol{\Sigma}_\boldsymbol{k}^{-1}\left(\boldsymbol{d}_k - \hat{\boldsymbol{d}}_k\right)\right). \tag{13}$$

Once a set of mathematical expressions for the prior and likelihood densities has been established as above, we may select a suitable algorithm to characterise the posterior space. The Metropolis-Hastings algorithm is one of the most common methods for doing so and involves generating a chain of models with associated posterior density values (Metropolis et al., 1953).

Given a current model $\boldsymbol{\mathcal{X}}^n$, a proposal model $\boldsymbol{\mathcal{Y}}^{n+1}$ is constructed according to the relationship

$$\boldsymbol{\mathcal{Y}}^{n+1} = \boldsymbol{\mathcal{X}}^n + \boldsymbol{\mathcal{P}}, \tag{14}$$

where $\boldsymbol{\mathcal{P}} \sim \mathcal{N}(\mathbf{0}, \boldsymbol{\Sigma}^{\text{proposal}})$ and $\boldsymbol{\Sigma}^{\text{proposal}}$ is a suitable $N_\text{p} \times N_\text{p}$ proposal sampling covariance matrix. For simplicity, this matrix is typically chosen to be diagonal. The proposal model is accepted with probability

$$a^n = \min\left(1, \frac{p(\boldsymbol{\mathcal{Y}}^{n+1}|\boldsymbol{\mathcal{D}})}{p(\boldsymbol{\mathcal{X}}^{n}|\boldsymbol{\mathcal{D}})}\right), \tag{15}$$

where a^n is known as the acceptance ratio and is calculated using equation (9). If the proposal model is accepted one sets $\boldsymbol{\mathcal{X}}^{n+1} = \boldsymbol{\mathcal{Y}}^{n+1}$. Otherwise the current model remains and one sets $\boldsymbol{\mathcal{X}}^{n+1} = \boldsymbol{\mathcal{X}}^{n}$. This process is repeated until the parameter space is suitably explored. Since the probability of a model being accepted is proportional to its posterior density, convergence towards optimal regions of the parameter space occurs. However, less probable models still have a finite acceptance probability, meaning the procedure is also capable of escaping local minima. To circumvent the issue that the evolution of samples is, at first, correlated with the initial starting point, the first 50% of trials are discarded as a so-called "burn-in" period. Only the post burn-in set of samples are used in the analysis.

While powerful, in our case, the Metropolis-Hastings algorithm in its original form is not sophisticated enough to perform the inversion efficiently, since strong trade-offs between model parameters invalidate the use of a diagonal proposal covariance matrix. The precise form of $\boldsymbol{\Sigma}^{\text{proposal}}$ has a strong impact on the average model acceptance rate a, which is optimised when $a \approx a^*$, where $a^* = 0.234$ (Gelman et al., 1997). When $\boldsymbol{\Sigma}^{\text{proposal}}$ is too small, a large proportion of models are accepted but only small steps around the model space are taken. When $\boldsymbol{\Sigma}^{\text{proposal}}$ is too large, only a small proportion of models are accepted and so the inversion algorithm tends to sample the same area of the model space for a prohibitively large number of trials, before wildly jumping elsewhere. This applies when any region of the multi-dimensional proposal covariance space is poorly estimated. Both situations lead to inefficient convergence towards the posterior distribution and so, for a finite number of trials, inhibit our ability to achieve a useful result. We therefore adopt the Global Adaptive Scaling Within Adaptive Metropolis (GASWAM) modification of Metropolis-Hastings (Andrieu et al., 2008; Figure 3; see Appendix C for methodological details).

There are two practical ideas underpinning the GASWAM algorithm. The first is that the most efficient choice of proposal covariance matrix, $\boldsymbol{\Sigma}^{\text{proposal}}$, is a scalar function of the model covariance matrix $\boldsymbol{\Sigma}^{\boldsymbol{\mathcal{X}}}$. The second is that $\boldsymbol{\Sigma}^{\boldsymbol{\mathcal{X}}}$ can be estimated for a given trial, n, of the inversion from the complete history of all preceding trials, $\{0, 1, \ldots, n-1\}$, using the formula

$$\boldsymbol{\Sigma}^{\boldsymbol{\mathcal{X}}} \approx \frac{1}{n-2}\sum_{i=1}^{n-1}\left(\boldsymbol{\mathcal{X}}^i - \overline{\boldsymbol{\mathcal{X}}}\right)\left(\boldsymbol{\mathcal{X}}^i - \overline{\boldsymbol{\mathcal{X}}}\right)^T, \tag{16}$$

where $\overline{\boldsymbol{\mathcal{X}}}$ is the iteratively updated average model

$$\overline{\boldsymbol{\mathcal{X}}} = \frac{1}{n-1}\sum_{i=1}^{n-1}\boldsymbol{\mathcal{X}}^i. \tag{17}$$

The GASWAM algorithm makes use of this empirically calculated covariance structure and an associated scale factor to progressively update the proposal covariance matrix. By simultaneously updating the shape and size of

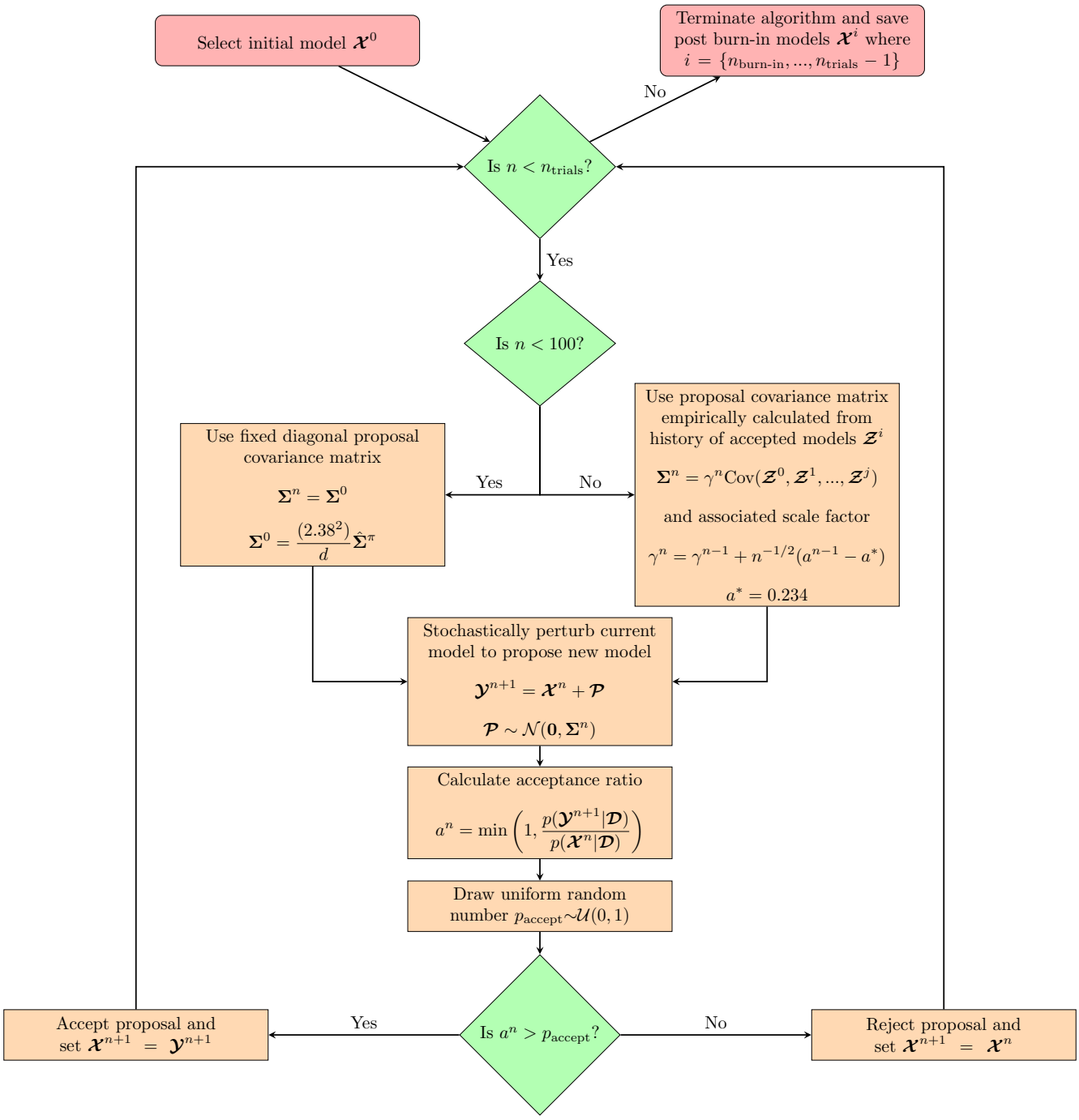

Figure 3: **Flow chart representation of the Globally Adaptive Scaling Within Adaptive Metropolis (GASWAM) adaptation (Andrieu et al., 2008) of the Metropolis-Hastings algorithm (Metropolis et al., 1953)**. Optimal acceptance ratio, $a^* = 0.234$, from Gelman et al. (1997). Initial proposal sampling covariance matrix based on the proposition of Haario et al. (2001). Algebraic superscripts refer to a particular choice of model.

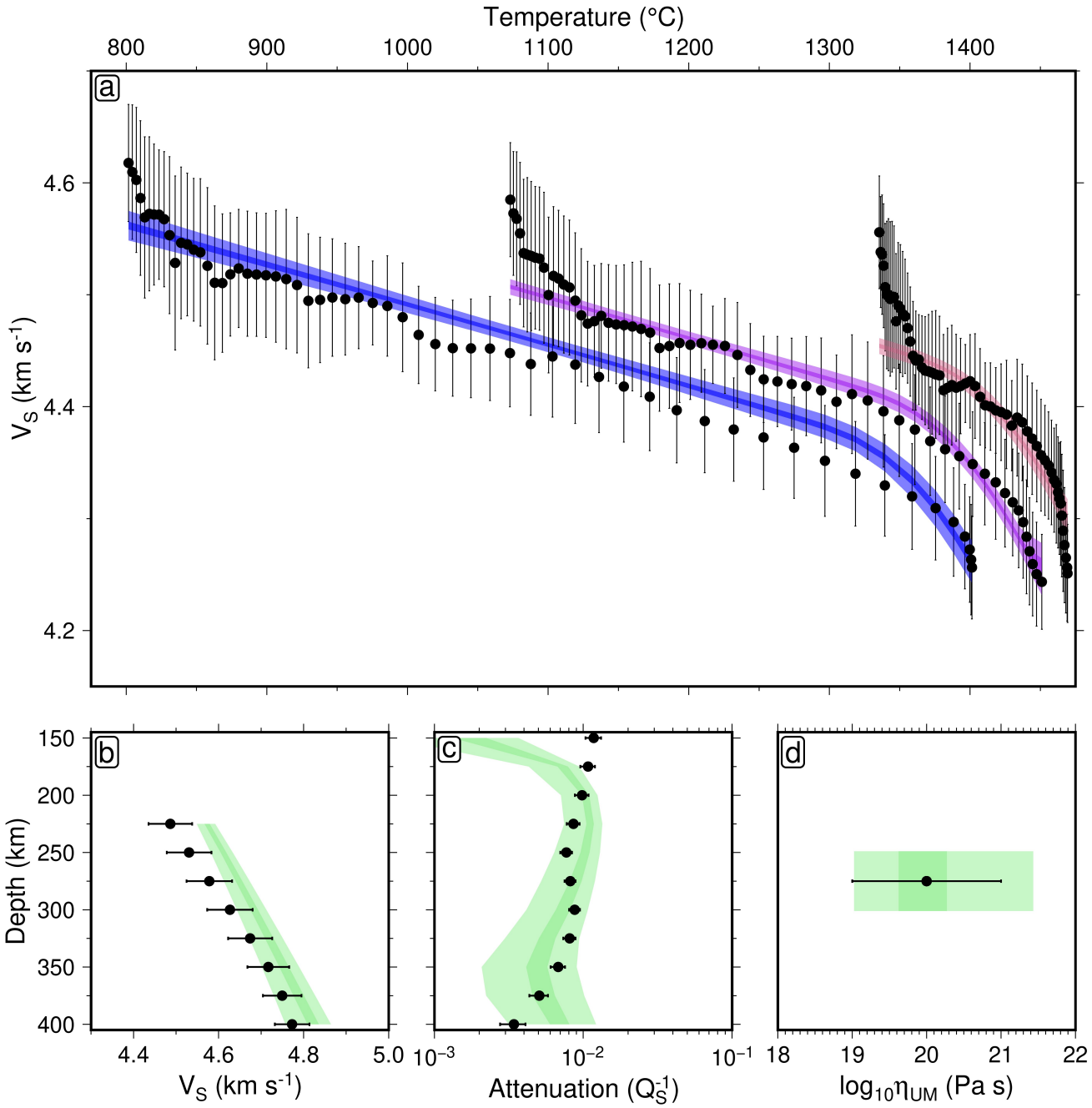

Figure 4: **Assessing fit of inverted anelasticity model parameters.** Fit of post burn-in models to the four geophysical data sets used to constrain the inversion procedure (circles/error bars; see Section 2.1). Pale shaded regions represent the 99% credible interval, and dark shaded regions represent the 50% credible interval. (a) Plate cooling model fit for depth ranges 50 to 75 km (blue), 75 to 100 km (purple) and 100 to 125 km (red). (b) Adiabatic model fit for depth range 225 to 400 km. (c) QRFSI12 seismic attenuation model fit at depths 150 to 400 km beneath ocean floor for ages $\geq$ 100 Ma. (d) Average viscosity between 225 to 400 km compared to $\eta = 10^{20\pm1}$ Pa s estimate.

the proposal covariance matrix, stabilisation of the inversion procedure can be achieved by enforcing the optimal acceptance ratio, such that $a \approx 0.234$. This stability is ensured by looking at a suite of convergence diagnostics including the running mean of each parameter as the trial proceeds, frequency density plots of each parameter, the potential scale reduction factor (Gelman et al., 1997; Roy, 2020), and the fit of the models to the data (Figure 4). The performance of the inversion algorithm was also tested against synthetic data, verifying that it behaved as expected (see Supporting Information for details).

The result of the inversion is a set of post burn-in models, $\boldsymbol{\mathcal{X}}^{\text{posterior}}$. This serves as a discrete set of sam-

ples over the continuous posterior density function, $p(\boldsymbol{\mathcal{X}}|\boldsymbol{\mathcal{D}})$. A greater sampling density is indicative of a more probable region of the model space. Since the sampled posterior distribution (ignoring hyperparameters) is seven-dimensional, it cannot be visualised as a whole. Instead, we calculate the sampling density for each combination of model parameters, $\mathcal{X}_i$ and $\mathcal{X}_j$. To achieve this, the posterior space of each parameter is discretised into $1,000$ blocks, spanning the range of values over which this parameter was sampled. This results in a step-size given by

$$h_i = \frac{\text{maximum}(\mathcal{X}_i) - \text{minimum}(\mathcal{X}_i)}{1000}. \tag{18}$$

The sampling density is then calculated as

$$\rho_{ij}\left(x, y\right) = n_{ij}\left(x, y\right) / A_{ij}, \tag{19}$$

where (x, y) is the grid reference pertaining to each of the $1,000 \times 1,000$ density values and $A_{ij} = h_i h_j$ the corresponding area.

To yield further information from the inversion output, the model samples and their corresponding physical predictions must be summarised mathematically. The expectation value of each parameter can be estimated using the discrete summation

$$\hat{E}(\mathcal{X}_i) = \frac{1}{N_s} \sum_{j=1}^{N_s} \mathcal{X}_i^j, \tag{20}$$

where N_s is the number of discrete model samples (Gallagher et al., 2009). The corresponding variance of each parameter may be estimated using the formula

$$\hat{V}(\mathcal{X}_i) = \frac{1}{N_s - 1} \sum_{j=1}^{N_s} \left(\mathcal{X}_i^j - \hat{E}(\mathcal{X}_i)\right)^2. \tag{21}$$

However, the vectors $\hat{\boldsymbol{E}}(\boldsymbol{\mathcal{X}})$ and $\hat{\boldsymbol{V}}(\boldsymbol{\mathcal{X}})$ do not tell the full story. The anelasticity model $\boldsymbol{\mathcal{X}}$ serves as a means for converting V_S into physical predictions of temperature, T, viscosity, η, and density, ρ. We are therefore interested in estimating the expectation value and variance of functions of the model $f(\boldsymbol{\mathcal{X}})$, rather than the model itself. This can be achieved easily, by constructing a vector, $\boldsymbol{\mathcal{F}}$, where each component is calculated according to the formula

$$\mathcal{F}^i = f(\boldsymbol{\mathcal{X}}^i). \tag{22}$$

The expectation value and variance of the physical prediction can be estimated analogously to equations (20) and (21), resulting in the equations

$$\hat{E}(\mathcal{F}) = \frac{1}{N_s} \sum_{j=1}^{N_s} \mathcal{F}^j, \tag{23}$$

and

$$\hat{V}(\mathcal{F}) = \frac{1}{N_s - 1} \sum_{j=1}^{N_s} \left(\mathcal{F}^j - \hat{E}(\mathcal{F})\right)^2. \tag{24}$$

The estimates for the expectation value, $\hat{E}(\mathcal{F})$, and variance, $\hat{V}(\mathcal{F})$, are referred to as the average and uncertainty,

respectively. If it is not practical to calculate all N_S values of $\mathcal{F}^i$, due to computational expense, a subset N_U of the overall set of post burn-in models may be used (see Section 4). The relationship between the uncertainty on a physical prediction, $\hat{V}(f(\boldsymbol{\mathcal{X}}))$, and the uncertainty on the underlying model parameters, $\hat{\boldsymbol{V}}(\boldsymbol{\mathcal{X}})$, is dependent on the sensitivity of $f(\boldsymbol{\mathcal{X}})$ to each parameter, $\mathcal{X}_i$ (i.e., the gradient, $\partial f(\boldsymbol{\mathcal{X}})/\partial \mathcal{X}_i$), and the covariance structure of the model, $\boldsymbol{\Sigma}^{\boldsymbol{\mathcal{X}}}$ (Champac et al., 2018). In the case of the anelasticity parameterisation, $T(\boldsymbol{\mathcal{X}})$ and $\eta(\boldsymbol{\mathcal{X}})$ are non-linear functions of V_S, complicating the analytical calculation of their expectation value and variance. This highlights one of the key benefits of taking a Bayesian approach, as it provides a simple way of propagating uncertainties, using the discrete summaries of equations (23) and (24).

3 Anelasticity model covariance structure

Posterior sampling densities for each parameter combination highlight clear trade-offs, as expected given our need to adapt the proposal sampling scheme to handle non-diagonal model covariance structure (Figure 5). We find that the anelasticity model $\boldsymbol{m}$ can be approximately separated into two independent components, $\boldsymbol{A} = \{\mu_0, \partial\mu/\partial T, \partial\mu/\partial P\}$ and $\boldsymbol{B} = \{\eta_0, E_A, V_A, \partial T_S/\partial z\}$, such that $\boldsymbol{m} = \{\boldsymbol{A}, \boldsymbol{B}\}$. A reasonable approximation for the model covariance structure therefore takes the form

$$\boldsymbol{\Sigma}^{\boldsymbol{\mathcal{X}}} \approx \begin{bmatrix} \boldsymbol{\Sigma}^{\boldsymbol{A}} & \mathbf{0} \\ \mathbf{0} & \boldsymbol{\Sigma}^{\boldsymbol{B}} \end{bmatrix}. \tag{25}$$

There exist strong parameter trade-offs within $\boldsymbol{A}$ and $\boldsymbol{B}$ separately, but only weak trade-offs between $\boldsymbol{A}$ and $\boldsymbol{B}$. This is in accordance with what we expect physically, whereby $\boldsymbol{A}$ regulates the elastic component of the physical response, and $\boldsymbol{B}$ the transient component.

Within $\boldsymbol{A}$, we observe a very strong negative trade-off between the reference shear modulus and its temperature derivative. This implies that with respect to the maximum *a posteriori* estimate for this combination of parameters, a similar fit to the data can be obtained by co-varying μ_0 and $\partial\mu/\partial T$ in opposite directions. It is possible to verify that this makes sense in the context of the plate model $V_S(T)$ relationship (Figure 4a), which serves as the main data constraint on the inversion, as follows. The linear region of the $V_S(T)$ relationship in a given depth bin is well-approximated by assuming an elastic response at fixed pressure, and may therefore be expressed as (Appendix D)

$$V_S(T) \approx \sqrt{\frac{\mu_0^*}{\rho}} - \sqrt{\frac{\left|\partial\mu/\partial T\right|^2}{4\mu_0^*\rho}}\,(T - T_0)\,. \tag{26}$$

Therefore, an increase in the reference shear modulus has the effect of increasing the V_S value at which the $V_S(T)$ trend is initialised, as well as reducing the absolute gradient of the trend. The temperature gradient of the shear modulus must assume a correspondingly more negative value to compensate, in order to preserve the squared distance between data and model. A symmetric argument can be used to interpret the positive trade-off between reference shear modulus and its pressure gradient. The relative weakness of this $\left(\mu_0, \partial\mu/\partial P\right)$ trade-off compared to that of $\left(\mu_0, \partial\mu/\partial T\right)$ may, in part, be down to the lower level of information that our data set contains on the variation of V_S with depth. In addition, a negative trade-off between the temperature and pressure derivatives of

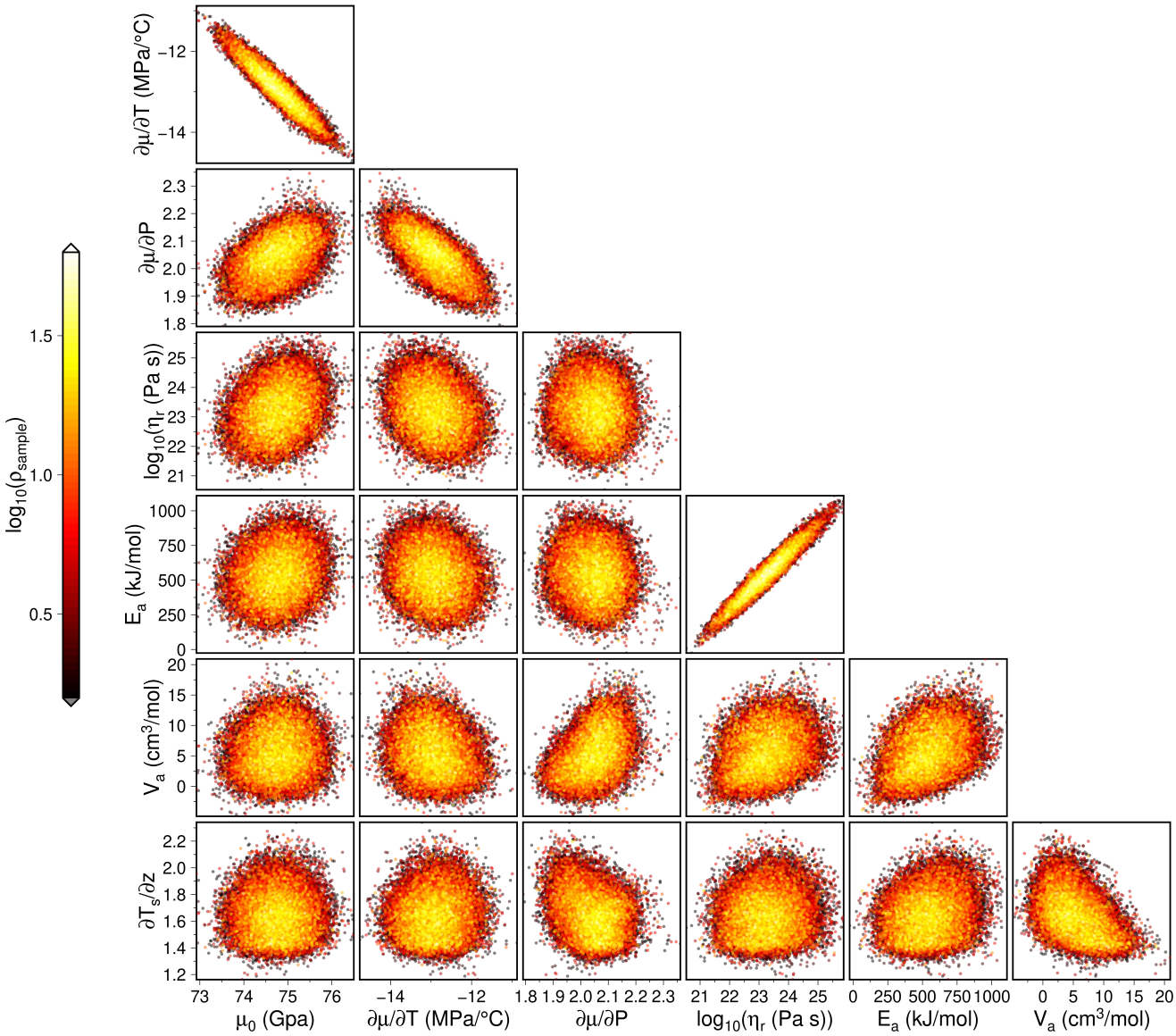

Figure 5: **Posterior distributions of model parameters.** Posterior sampling density (ρ, arbitrary units) of each combination of anelasticity models, highlighting physical trade-offs between parameters.

the shear modulus appears to be present.

By far the strongest parameter trade-off observed within the anelasticity model is contained within $\boldsymbol{B}$, between activation energy and reference viscosity; parameters controlling the onset and strength of anelastic effects respectively. The non-linear relationship between parameters in the anelastic regime prevents an analytical derivation of the trade-off between E_A and η_0. However, it appears that while the individual uncertainties on E_A and η_0 are very large, the strength of trade-off between the two ensures only a small variation in the misfit between data and model. Trade-offs between other parameters within $\boldsymbol{B}$ appear to be present, although relatively weak. In order to further constrain the model covariance, more data containing information about anelastic behaviour, especially at high pressure, are required.

4 Predictions of thermomechanical structure beneath Antarctica

Given a depth slice of ANT-20, it is possible to convert each $V_S(\theta, \phi)$ value into an estimate of thermomechanical state (viscosity, η, temperature, T, and density, ρ) by assuming a choice of anelasticity model $\boldsymbol{\mathcal{X}}^i$. To assess the improvement achieved by using the inversion procedure to refine this choice of model, we present a series of three mean and standard deviation viscosity structures, each calculated based on the 150 km depth slice of ANT-20 (Figure 7). In each case, we select N_U anelasticity models, summarising the results by substituting $\log_{10}\eta$ into equations (23) and (24). This results in a geometric mean and standard deviation of the viscosity at each location. In case I, each parameter is sampled independently from the prior distribution (Table 1). This represents, conservatively, the quality of Antarctic viscosity prediction that we can make based purely on experimental data pertaining to the mechanical behaviour of the upper mantle. In case II, each parameter is sampled independently from the posterior distribution (Table 1). This represents the quality of prediction it is possible to make having calibrated the anelastic parameters with independent geophysical data, but ignoring any information on the covariance between parameters. Finally, in case III, the optimal approach laid out in Section 2.2 is taken, using a uniform random sample of posterior anelasticity models from the full set of $N_S = 200,000$ post burn-in models. This represents our best constraint on viscosity structure, including not only the refinement of individual parameters based on the data, but also information that the data provides about the model covariance structure. The use of a subset of the post burn-in models ensures computational viability. A suitable value for the sieving ratio N_U/N_S, representing the proportion of total post burn-in models used at the prediction stage, was found by investigating the additional information obtained by increasing N_U in integer steps, starting at 1 (Figure 6). It was ascertained that N_U as small as 100 was sufficient to bring deviations in the mean and standard deviation viscosity structure down to a fraction of a percentage upon the addition of an extra anelasticity model, and therefore a safe choice of $N_U = 1,000$ was taken.

A large reduction in uncertainty (4 to 5 orders of magnitude) is observed from case I-III (Figure 7; panels b, d, f), highlighting the benefit of the inversion as a whole. The most dramatic improvement occurs between case II

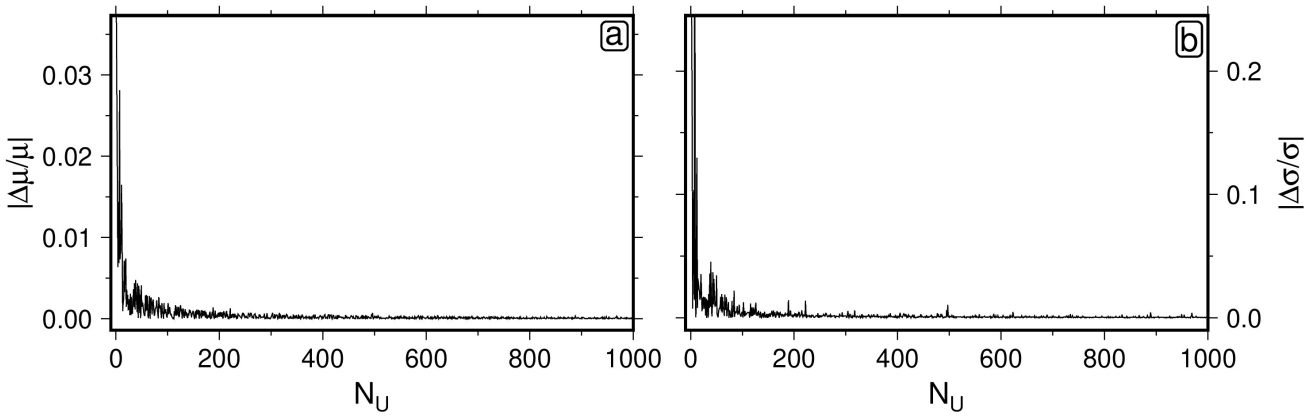

Figure 6: **Determining the number of models required to accurately characterise posterior expectation and variance.** Stability of the expectation value μ, and the uncertainty σ, of predicted viscosity at an arbitrary location ($z = 150$ km, longitude $\theta = 0.00°$, latitude $\phi = -90.00°$) of the ANT-20 V_S model, as a function of the number of randomly selected posterior anelasticity models used to construct them, denoted by N_U. Calculated by looking at the discrepancy in a physical prediction, X, before and after introducing an extra model, $(\hat{X}(n+1) - \hat{X}(n))/\hat{X}(n+1)$. (a) $X = \mu$. (b) $X = \sigma$.

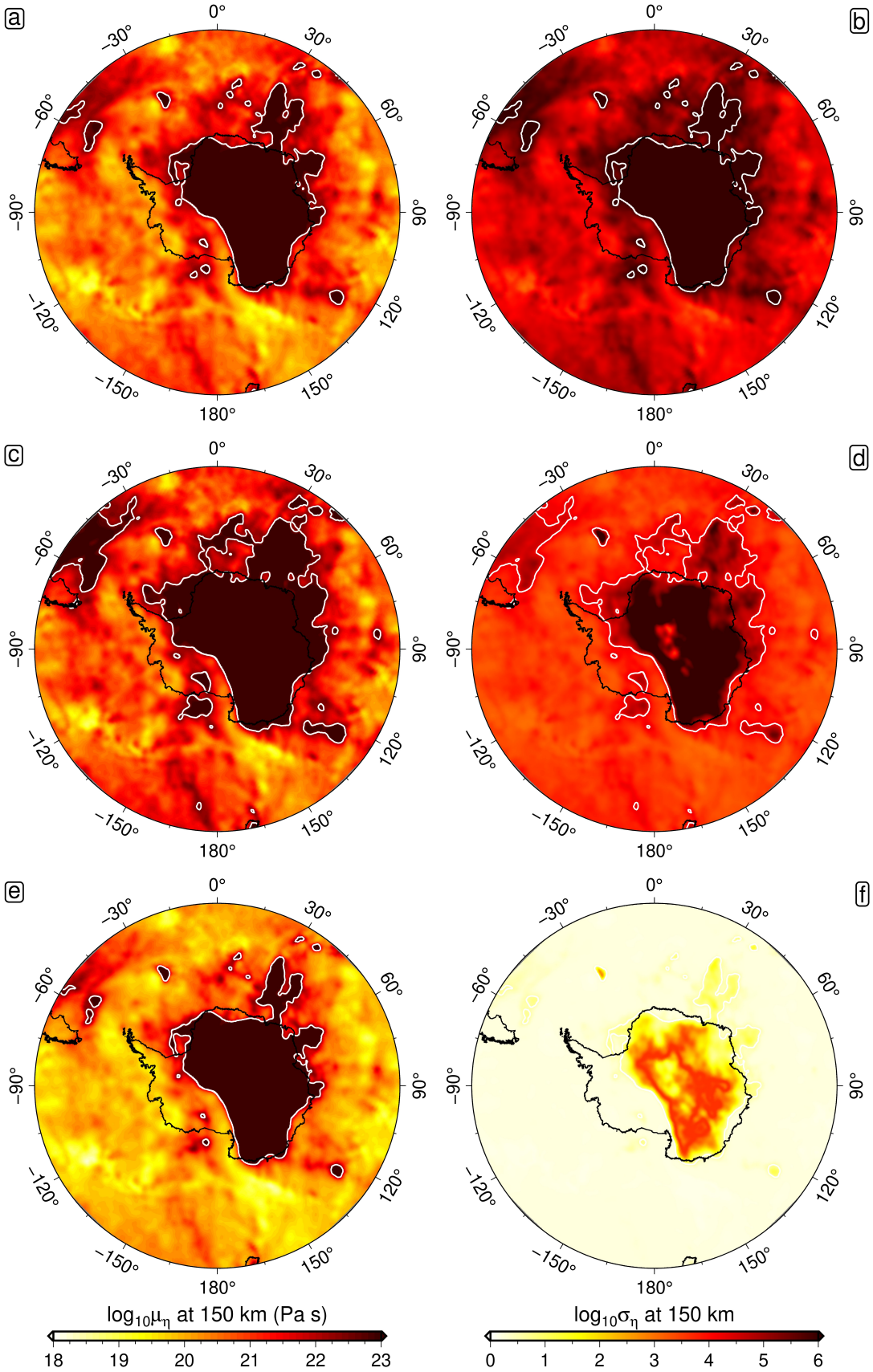

Figure 7: **Diffusion creep viscosity and uncertainty based on forward and inverse modelling.** Geometric mean (left-hand column; panels a, c, e) and standard deviation (right-hand column; panels b, d, f) viscosity structure at 150 km, calculated using three different methods. First (top row; panels a, b), by sampling anelasticity parameters independently from the prior distribution (see Table 1). Secondly (middle row; panels c, d), by sampling anelasticity parameters independently from the posterior distribution. Finally (bottom row; panels e, f), by sampling sets of anelasticity parameters from the posterior output. In each case, $N_U = 1,000$ models are used to generate the ensemble of viscosity predictions. White contours denote regions in which mean viscosity $\mu_\eta > 10^{22.5}$ Pa s.

and III, due to the effect of the highly non-diagonal covariance structure, which, due to compensation, results in muted variation in physical predictions for posterior models that encompass wide parameter ranges. Constraining the covariance structure of the physical model used to convert between shear-wave velocity and thermomechanical parameters is therefore central to the quality of the result we obtain. As a result, complementary data sets such as those used to calibrate the inversion here are hugely important. We may conclude from this assessment that the statistical inverse framework, as utilised optimally in Case III, provides the basis for improved predictions of thermomechanical structure. Therefore, this approach is taken to calculate a range of physical outputs in the results that follow.

4.1 Viscosity structure

The diffusion creep viscosity structure derived from the application of our conversion method to the ANT-20 V_S model contains significant lateral heterogeneity beneath the Antarctic continent and surrounding oceans. This is to be expected given the presence of shear-wave velocity anomalies up to 8% in relative amplitude observed in the underlying tomography (see Lloyd et al. (2020); Figure 11). To show how this behaviour manifests itself in terms of viscosity variation, we calculate geometric mean and standard deviation viscosity structures as a function of depth (Figures 8 and 9). Note that at low homologous temperatures, the anelastic contribution to V_S variation is negligible, meaning that viscosities cannot be reliably constrained when $\eta > 10^{22.5}$ Pa s (white contours in Figures 8 and 9). However, this is an issue of minor significance, since regions with viscosities above this threshold have Maxwell relaxation times exceeding 20 kyr and will behave elastically over the timescales relevant to GIA modelling. In the analysis that follows, we define the asthenosphere as the region in which $\eta < 10^{22.5}$ Pa s.

At 150 km depth, the thermomechanical dichotomy between East and West Antarctica is most obvious; a sharp viscosity boundary follows the path of the Transantarctic Mountain Range (TAM) across the continent from the Ross to the Weddell Sea. The mantle at this depth is lithospheric beneath much of the EAIS, and asthenospheric beneath the WAIS. Within West Antarctica itself, viscosity varies within the range 10^{19-23} Pa s, and it is possible to identify two long-wavelength low-viscosity anomalies. The first arises at the Macquarie Triple Junction, extends to the Balleny Islands, and follows the TAM as it passes into West Antarctica through the western side of the Ross Embayment. The second passes from Marie Byrd Land, through the Amundsen Sea Embayment, to the Antarctic Peninsula. Both anomalies contain viscosities as low as $\eta \sim 10^{19}$ Pa s, and are also identifiable at 75 km, where they form a connected region which is the only portion of asthenosphere within the continental footprint at this depth. Model-based uncertainty in asthenospheric viscosity is very low (~ 0.25 orders of magnitude) at 75 km and 150 km depth, and appears mostly homogeneous, albeit increasing appreciably within localised regions of very high viscosity. Given the small size of these regions (e.g., the higher viscosity patch beneath Marie Byrd Land at 150 km depth), it is difficult to rule out the possibility that they are they result from tomographic artefacts.

At deeper depths (250 km and 350 km), average asthenospheric viscosities within the continent are higher ($\overline{\eta} = 10^{20.5\pm0.5}$ Pa s and $\overline{\eta} = 10^{21.4\pm0.6}$ Pa s, in terms of median and median absolute deviation, respectively) and the area of lithospheric coverage is reduced, leading to an overall more homogeneous structure. The low-viscosity anomaly observed at shallow depths beneath the Antarctic Peninsula has evolved into a high-viscosity anomaly

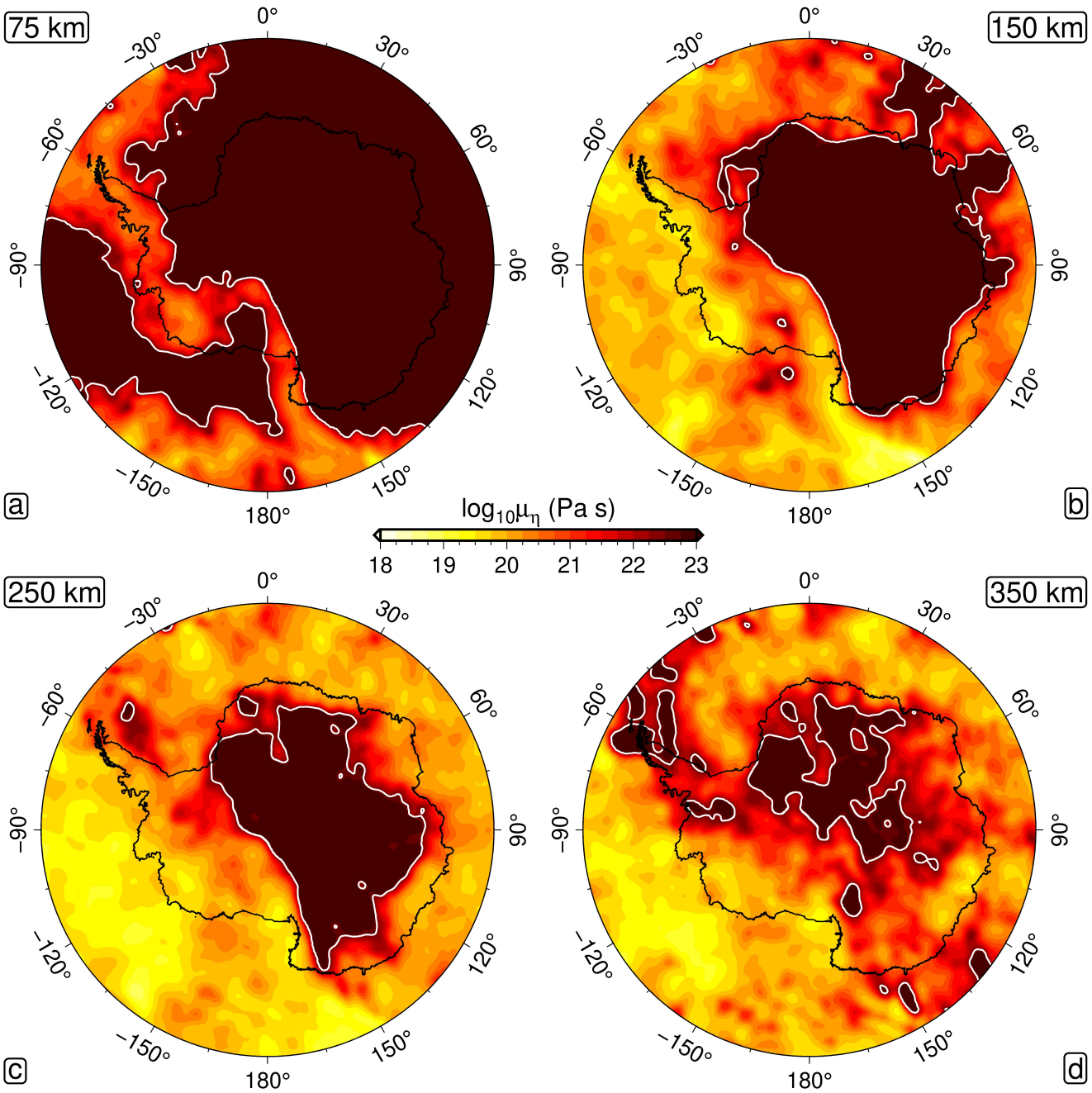

Figure 8: **Diffusion creep viscosity beneath Antarctica.** Geometric mean viscosity structure at 75 km, 150 km, 250 km and 350 km depth (a, b, c and d, respectively). Each structure is calculated by utilising a uniform random sample of $N_U = 1,000$ posterior anelasticity models to convert ANT-20 shear-wave velocities into viscosity, and averaging the resulting ensemble.

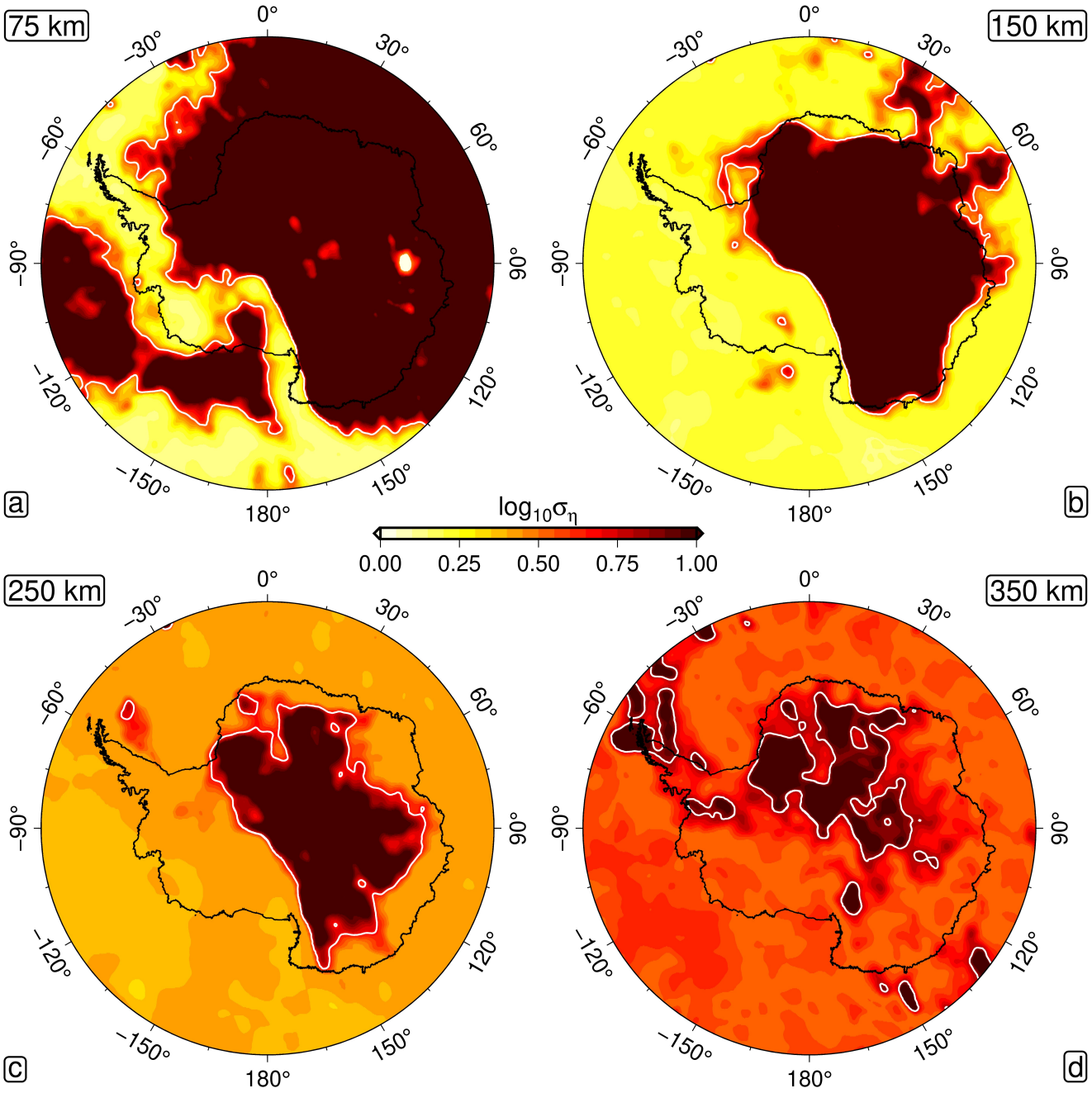

Figure 9: **Uncertainty in diffusion creep viscosity beneath Antarctica.** Geometric standard deviation viscosity structure at 75 km, 150 km, 250 km and 350 km depth (a, b, c and d, respectively). Each structure is calculated by utilising a uniform random sample of $N_U = 1,000$ posterior anelasticity models to convert ANT-20 shear-wave velocities into viscosity in terms of, and determining the variance of the resulting ensemble.

that extends towards the South Scotia ridge by a depth of 350 km, possibly representing a fossil slab (An et al., 2015). Low viscosity regions present beneath the Ross and Amundsen Sea Embayments at 150 km persist at these depths, although the high viscosities that separate the two regions at shallower depths appear muted or absent. In addition, a large low viscosity anomaly can be seen in the Southern Ocean in the vicinity of Marie Byrd Land, consistent with the presence of a mantle plume (Seroussi et al., 2017). Average asthenospheric viscosity uncertainty increases with depth, likely reflecting the lack of deep geophysical data used to constrain the inversion for material properties. In particular, the inversion procedure is unable to constrain activation volume beyond an individual parameter precision of approximately 10%. Since this parameter governs the pressure-dependence of viscosity, deep viscosity uncertainty is highly correlated with activation volume uncertainty. However, lateral variations in uncertainty structure remain minimal, and even at 350 km depth do not exceed an order of magnitude.

4.2 Lithosphere-asthenosphere boundary depth

The framework used to construct self-consistent predictions of thermomechanical structure beneath Antarctica can also be utilised to constrain other parameters important for GIA and ice-sheet modelling studies. First, we utilise the ensemble of 3D temperature structures to infer lithosphere-asthenosphere boundary (LAB) depth. For each temperature structure associated with a given choice of anelasticity model in the ensemble, the laterally varying geothermal profiles are interpolated to a 1 km depth interval. Prior to interpolation, anomalous temperatures associated with downward bleeding of crustal velocities in the underlying tomography are removed by identifying spurious reversals of the geothermal gradient and excising temperatures above these loci. In all cases, a temperature of 0°C is enforced at the basement depth. Following interpolation, we extract the depth at which the resulting profile intersects a temperature of 1200°C, a proxy for LAB depth (Figure S5, Burgos et al., 2014; Richards et al., 2018). By summarising the set of ensemble predictions of laterally varying LAB depth, according to equations (23) and (24), we arrive at a mean and standard deviation LAB depth structure (Figure 10).

The resulting mean LAB depth displays a number of interesting features. We find good agreement with long-wavelength structure observed elsewhere in the literature (Priestley et al., 2018; Richards et al., 2020b), whereby LAB depth exceeds 150 km beneath the EAIS, and is much lower beneath the WAIS. We find spatially averaged LAB depths of 233 ± 41 km and 63 ± 13 km beneath the respective ice sheets, calculated according to the median and median absolute deviation. The overall strength of this heterogeneity is high, involving LAB depths as shallow as 40 km in the West, and as deep as 360 km in the East. The full distribution of LAB depths represented by East and West Antarctica are shown in Figure 11, along with the classification used to distinguish between the two continental components, which is based on the satellite-mapped drainage network (Zwally et al., 2012).

The maximum ~ 15 km depth resolution and ~ 100 km lateral resolution of the underlying tomography is the dominant source of uncertainty on the calculated LAB structure over much of Antarctica, as a result of the low variance in LAB depth predictions provided by the ensemble of anelasticity models. However, this is not the case in certain areas of East Antarctica, where very large inferred LAB depths are also associated with large uncertainties, of order 30 to 40 km. The statistical uncertainty associated with the ensemble of anelasticity models is expected to rise with increasing LAB depth due to elevated temperature uncertainty with depth arising from the previously

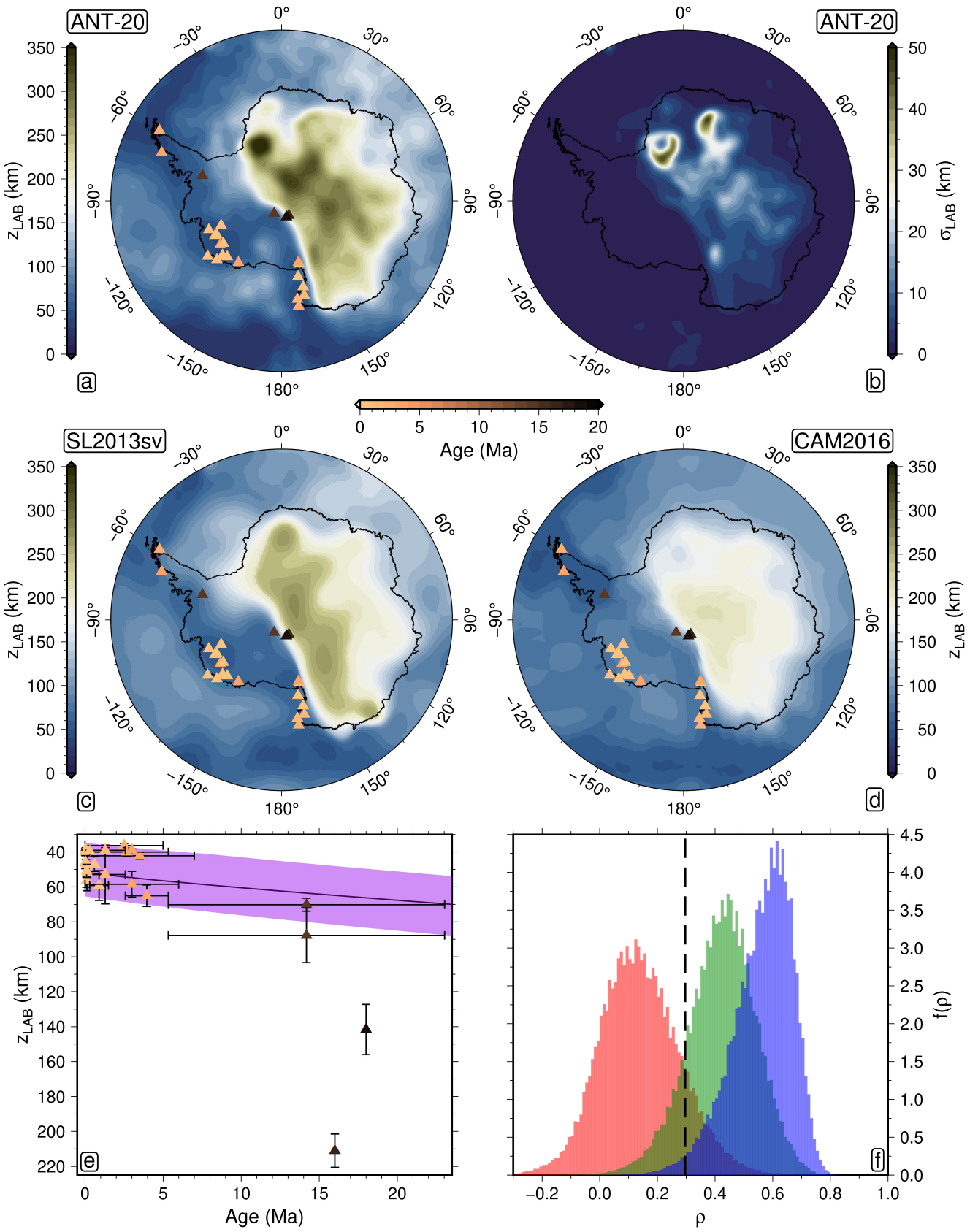

Figure 10: **LAB depth variations beneath Antarctica.** Mean (a) and standard deviation (c) [swap b and c?] lithosphere-asthenosphere boundary (LAB) depth derived from ANT-20, as estimated from depth to the 1200°C isotherm. ANT-20-derived LAB structure is compared to the predictions of Richards et al., 2020b (c) and Priestley et al., 2018 (d), derived from the SL2013sv and CAM2016 seismic tomography models, respectively. The LAB depth models are overlain with the minimum age since last continental magmatic activity; the relationship between these two variables is shown for ANT-20 in (e). Histogram (f) displays the distribution of possible Spearman's Rank correlation coefficient values, ρ, between LAB depth and age for each LAB structure (CAM2016 - red, ANT-20 - green, SL2013sv - blue). Black dashed line = minimum value of ρ required for there to be a statistically significant increase in LAB depth with age at the 95% confidence level.

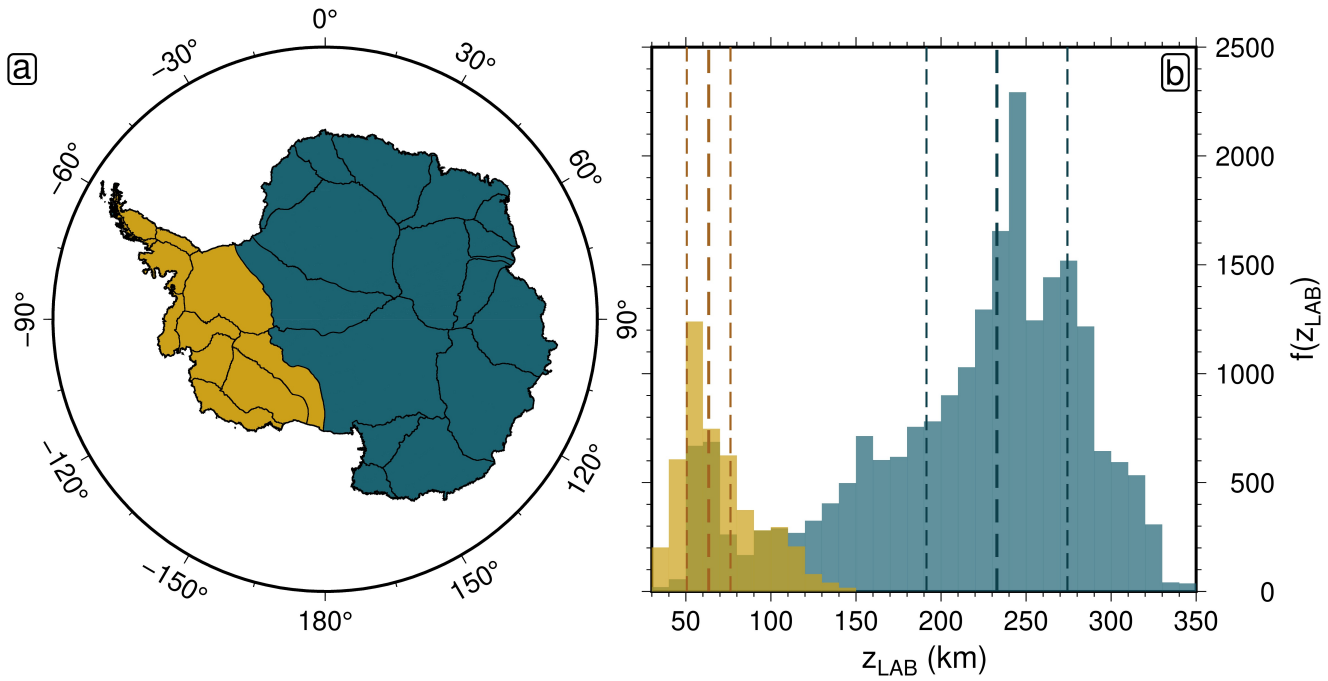

Figure 11: **Antarctic LAB depth dichotomy.** (a) Drainage network divides developed by the Goddard Ice Altimetry Group from ICESat data (Zwally et al., 2012). (b) Distribution of LAB depths beneath WAIS and EAIS (yellow and blue, respectively).

discussed uncertainty in activation volume.

By comparing the predictions made from our model of LAB depth to geological constraints not linked to the anelasticity calibration procedure, it is possible to verify that the temperature structures arrived at via the inversion method are realistic. We looked at the location and timing of Cenozoic magmatism, using a compilation of geochemical analyses on volcanic material (Sarbas, 2008; Ball et al., 2021). The data were spatially binned over a length scale of 100 km, in accordance with the seismological resolution, with minimum time since last eruption and its associated uncertainty extracted. The data were further processed to remove points with age uncertainties exceeding 10 Ma and the resulting data set mapped (Figure 10). Two key observations are immediately apparent when comparing magmatism and LAB depth. First, all sites containing a record of Pliocene or Quaternary (i.e., 5.33 Ma to present) eruptions lie above ANT-20 derived LAB depths in the range 35 to 70 km; the shallowest continental depths predicted by the present day seismic structure. This result is consistent with geodynamic expectations, since for a reasonable range of mantle temperature and hydration conditions, significant decompression melting is only expected in regions with LAB depth shallower than 80 km (Ball et al., 2021). Secondly, the minimum age since last eruption falls within the Miocene epoch for the remaining four sites, and here, LAB depth exceeds 70 km. The lack of more recent magmatism in these regions indicates that the source of such magmatism has been removed over geological time scales. If this is the case, the lithosphere-asthenosphere boundary would have recovered to an equilibrium depth more representative of mean mantle conditions, thus further validating our model predictions.

To validate this hypothesis we use models of conductive cooling to determine the expected increase in LAB depth as a function of geological time. We adapt the thermal modelling approach of Richards et al. (2020a), imposing an initial temperature condition that assumes a steady-state geotherm has been established by the time active magmatism ceases. We test a range of initial geotherms with 1358–1507°C mantle potential temperatures,

35–65 km initial LAB depths, and 10–40 km crustal thicknesses, based on seismically inferred values beneath the Antarctic magmatic provinces. In all models we assume an equilibrium plate thickness of 250 km and, based on calculated relationships between potential temperature and time since last eruption, we assume that initial thermal anomalies decay linearly to ambient temperatures (1333°C) over a 15 Myr period (see Supporting Information for details). In order to compare the output of our conductive cooling models to the data, we tie the spatially binned eruption age values to a prediction of LAB depth and its uncertainty, calculated by taking the average and standard deviation of the depths within each bin (Figure 10e). The majority of the magmatic data are fully consistent with the post-magmatic lithospheric thickening models, suggesting that our seismically inferred LAB values are reliable. However, the LAB depth beneath the two oldest localities is significantly deeper than would be expected for a purely conductive control on lithospheric thickness evolution. One potential explanation for this apparent mismatch is that thin lithosphere may truly be present beneath these regions but we cannot detect its presence due to seismic resolution limitations and spatial aliasing of short-wavelength signals near the transition between thin lithosphere in the West and thick lithosphere in the East. Alternatively, it may be that this volcanic material, which is emplaced within the West Antarctic rift system, does not lie above the original site of magma generation. For example, in similar continental regions characterised by thick sedimentary basins and complex tectonic histories, inclined faults, changes in stress state, and permeability barriers can encourage lateral transport of magma within the subsurface, leading to eruption centres that are horizontally offset from melting sites by several hundred kilometres (Maccaferri et al., 2014; Magee et al., 2016). Seismically inferred LAB depths may therefore be entirely accurate in this region, with deviations from conductive cooling model expectations attributable instead to violation of the assumption that present-day volcanic centres overlie the original site of magma generation.

To further investigate whether our data implies the existence of a monotonic relationship between LAB depth and minimum age since last eruption, we applied a statistical test. A Monte Carlo approach was employed to simulate the distribution of possible trends according to the uncertainty reported on each LAB depth-age data point, as follows. For each data point, d_i, initially located at $d_i = (a_i, z_i)$ in age-depth space, a random perturbation, $\Delta_i = (\alpha_i, \zeta_i)$, is added by drawing from a normal distribution with diagonal covariance scaled by the location-dependent age and depth uncertainties. The resulting trend represents one possible combination of "true" age-depth values, and we calculate a corresponding Spearman's Rank correlation coefficient for this trend. This process is repeated until convergence, resulting in a distribution of possible correlation coefficients for each LAB depth model (Figure 10f). For us to associate a given coefficient with statistically significant evidence for the existence of a positive monotonic relationship between LAB depth and minimum age since last eruption at the 95% confidence level, it must exceed a value of $\rho = 0.296$.

We find that the ANT-20 and SL2013sv derived LAB models satisfy this test to at least the 1σ level, with coefficients $\rho = 0.42 \pm 0.12$ and $\rho = 0.56 \pm 0.10$ respectively. This result suggests that both models make reliable LAB depth predictions in the context of the geological record. It is unlikely however that the improved correlation offered by SL2013sv necessarily translates into this being a more realistic LAB model than ANT-20. This is because while, in each case, the spatial binning procedure was conducted over a 100 km radius, the true lateral resolution of SL2013sv is much poorer than ANT-20 over Antarctica. The resulting LAB model is therefore laterally

smoother, reducing spatially binned LAB depth uncertainties and potentially improving the average trend observed in the age-depth data. It is unlikely that the LAB model derived from CAM2016 satisfies our test for statistical significance, owing to a coefficient, $\rho = 0.14 \pm 0.14$, such that only around 10% of possible age-depth trends contain a statistically significant positive gradient. This result may indicate that the LAB depth predictions of CAM2016 are less reliable in the Antarctic region than its counterparts. Nevertheless, there are several limitations on this analysis imposed by the small size of the magmatic dataset, significant clustering of data points within age-depth space, and large age uncertainties on certain data points. These have a non-negligible impact on the calculated correlation coefficients, and so this analysis does not provide conclusive evidence for the reliability, or lack thereof, of any given seismologically derived LAB depth model.

4.3 Geothermal heat flow

In addition to calculating LAB depth, we constrain continental geothermal heat flow (GHF) by fitting a steady-state, laterally varying geotherm to our ensemble of 3D temperature structures following the procedure laid out in McKenzie et al. (2005). As in the construction of LAB depth estimates, anomalous temperatures associated with crustal bleeding were excised prior to interpolation of the geothermal profile back to 0°C at the basement depth (Figure S5). The Moho heat flux and mechanical boundary layer thickness are optimised based on the discrepancy between the modelled and V_S-derived geothermal profiles at each location, and the surface temperature gradient is utilised to calculate GHF. In constructing a modelled geothermal profile at a given location, it is necessary to account for variations in crustal thickness, radiogenic heat production, and conductivity with depth. We make use of the crustal thickness grid associated with the tomography, to ensure self-consistency. For crustal heat production, we assume a value of $H^*_{\text{cont}} = 1.0$ µW m^{-3} and $H^*_{\text{ocean}} = 0.0$ µW m^{-3} within the continent and ocean respectively, distributed uniformly throughout the crustal layer. Mantle and oceanic crust conductivity are calculated according to the temperature- and pressure-dependent parameterisation of Korenaga et al. (2016). In the continent, crustal conductivity is set to a constant value of $k_{\text{crust}} = 2.5$ W m^{-1} K^{-1}. These assumptions simplify the true lateral and depth dependence of heat production and conductivity within the continental crust, which are expected to vary within the range $H^*_{\text{cont}} \sim \{0.0, 3.0\}$ µW m^{-3} and $k_{\text{crust}} \sim \{1.0, 4.0\}$ W m^{-1} K^{-1} (Jennings et al., 2019). It is beyond the scope of this study to investigate the effect of the variation of these two parameters on the resulting heat flow. However, a close fit between theoretically and V_S-derived geothermal profiles calculated using our simple parameter assumptions suggests the dominant control on GHF estimates is the seismically inferred thermal structure rather than the chosen crustal parameterisation. With this in mind, we utilise a laterally varying mantle potential temperature during the fitting process, estimated according to the average V_S-derived temperature beneath the base of thermal boundary layer.

Resulting estimates of spatially averaged continental energy transfer rates are 57 ± 9 mW m^{-2} into the base of the EAIS, and 72 ± 6 mW m^{-2} into the base of the WAIS (Figure 12). Both sides of the continent contain GHF variations in excess of 40 mW m^{-2}. However, East Antarctica is less heterogeneous, with over 75% of its area characterised by GHF in the region 50 to 60 mW m^{-2}. A hot thermal anomaly located within the footprint of the Gamburtsev Mountain Range is observed, but only reaches approximately 70 mW m^{-2}. By contrast, the WAIS is

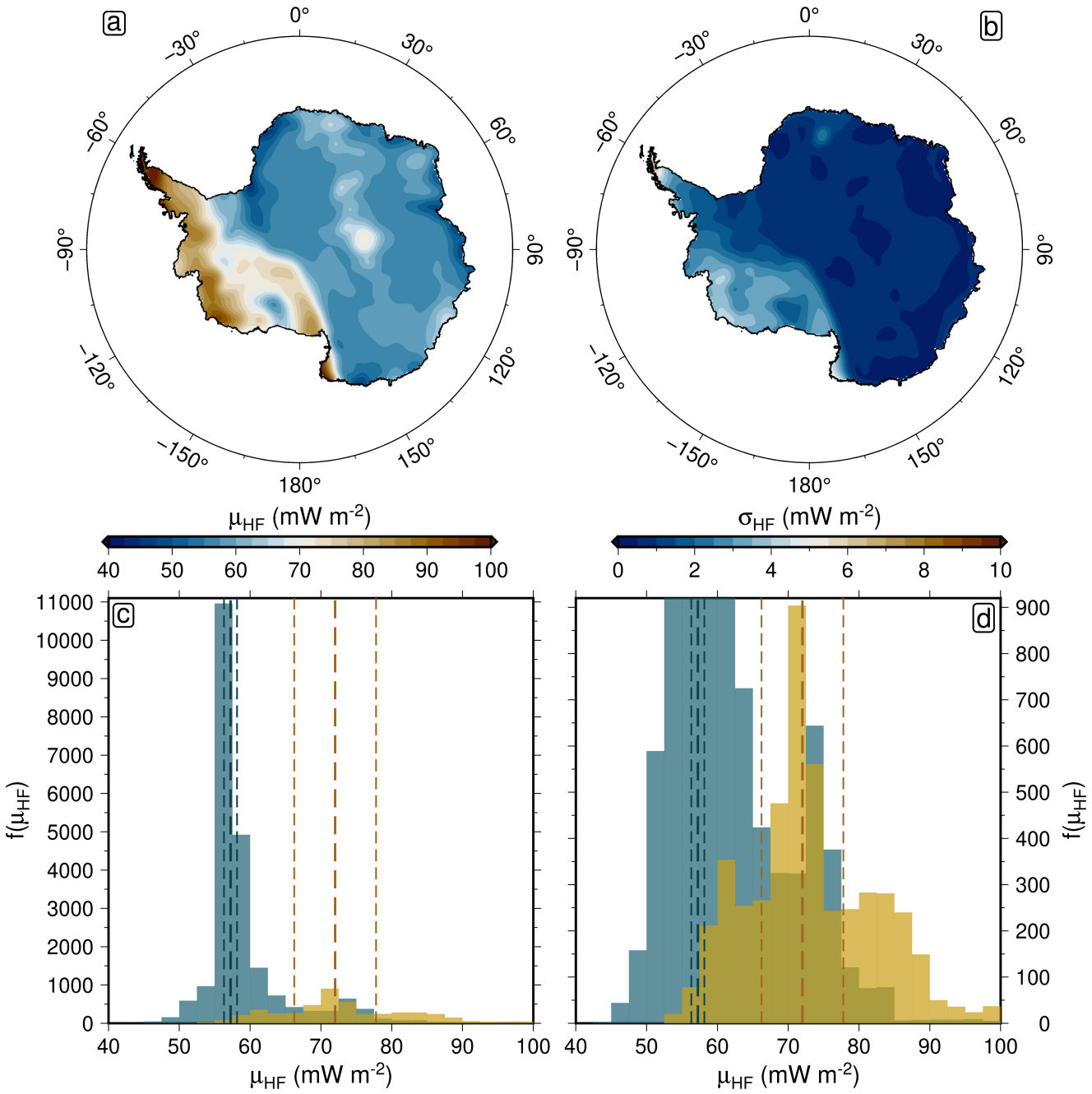

Figure 12: **GHF variations across Antarctica.** Mean (a) and standard deviation (b) geothermal heat flow derived from ANT-20. Estimated by fitting steady-state geotherms to temperatures inferred from an ensemble of anelasticity models. Distribution of geothermal heat flow into base of West Antarctic and East Antarctic Ice Sheets (c; yellow and blue, respectively). Zoom-in of distributions (d). Regional separation calculated according to the pattern of Antarctic drainage systems, see Figure 11. Thick dashed lines show the median of each distribution. Thin dashed lines are located one median absolute deviation away from the median of each distribution.

underlain by bedrock feeding it anywhere from 50 to 100 mW m^{-2} of geothermal energy, with heat flow unevenly distributed across the region. The connection of two long-wavelength (exceeding $10,000$ km) thermal anomalies into a single anomaly, observed in the viscosity structure at 75 km depth (Figure 8a), can also be seen here to stretch from the Ross Sea through Marie Byrd Land and up to the Antarctic Peninsula, before stretching offshore towards the South Scotia ridge. Most of this anomaly is located within West Antarctica, with the exception of its eastern edge within Marie Byrd Land and Victoria Land. The presence of this anomaly, combined with shorter-wavelength ($\sim$ 1,000–10,000 km) cold anomalies observed in Marie Byrd Land and Ellsworth Land, together make up a highly heterogeneous West Antarctic GHF structure.

5 Discussion

In the text to follow, we show how the results presented in this study build upon existing evidence of strong lateral heterogeneity in Earth's internal thermomechanical structure beneath Antarctica, leading to spatially variable lithosphere-asthenosphere boundary (LAB) depth and geothermal heat flow (GHF). First, the dichotomy between West and East Antarctic thermomechanical structure is discussed, along with implications for ice sheet stability. Secondly, our GHF predictions are compared to those of a recent study by Shen et al., 2020. Thirdly, we discuss how a consideration of physical forcing time scale can be used to reconcile observations and model predictions of mantle viscosity. Finally, we summarise the most significant sources of remaining uncertainty in quantifying mantle structure.

5.1 West and East Antarctic mantle structure

We find evidence that steady-state diffusion creep viscosities reach a lower threshold of $\eta \sim 10^{19}$ Pa s throughout the shallow mantle (150 to 350 km) beneath West Antarctica. Uncertainty in asthenospheric viscosity structure is found to be within one order of magnitude across the full depth range 0 to 400 km of study, and increases with depth. Low-viscosity anomalies observed within the mantle viscosity structure correspond with spatial patterns in LAB depth and GHF structure, whereby negative and positive anomalies are observed, respectively, which is to be expected given the self-consistent framework within which each of these parameters is estimated. For example, viscosities of $10^{19.5\pm0.3}$ Pa s present at 150 km depth in western Marie Byrd Land towards the Amundsen Sea Embayment are associated with thin LAB depths (50 ± 10 km) and elevated geothermal heat flow (90 mW m^{-2}). The inference that such low viscosities beneath the WAIS are caused by a thermal anomaly is consistent with the geological record of Cenozoic magmatism (Sarbas, 2008; Ball et al., 2021). The combination of high geothermal heat flow, thin lithosphere and low viscosity points to a highly dynamic ice sheet in regions including western Marie Byrd Land, the eastern Ross Embayment, and the Antarctic Peninsula. Large fluxes of thermal energy into the base of the ice sheet in these regions will likely enhance basal melting, reducing friction and increasing glacial sliding rates (Burton-Johnson et al., 2020; Shen et al., 2020). On the other hand, a thin lithosphere and low viscosity asthenosphere encourage rapid bedrock uplift and may help to stabilise and reduce grounding line retreat (Gomez et al., 2010).

We infer much higher viscosities beneath East Antarctica, with much of this side of the continent exhibiting LAB depths in excess of 150 km. LAB depth is on average 63 ± 13 km beneath West Antarctica, significantly lower than the 233 ± 41 km estimated beneath East Antarctica. The combination of thick lithosphere and moderate GHF suggest a less dynamic ice sheet. While there is evidence for a negative viscosity anomaly of order $10^{19.5 \pm 0.7}$ Pa s at a depth of 350 km beneath Wilkes Land, it does not penetrate up to shallower depths of 150 km, and therefore the influence of this anomaly on GIA rates is expected to be greatly reduced compared with the shallow anomalies beneath much of the WAIS. In addition, this region is associated with GHF of 60 to 70 mW m^{-2}. This is among the highest heat flow values estimated across East Antarctica (with the exception of the eastern Ross Embayment). Ice velocity and mass discharge rates across Wilkes Land are accelerating in response to warming temperatures in the Southern Ocean (Noble et al., 2020). The marine-based Aurora and Wilkes subglacial basins are positioned on a reverse bed slope, and may be susceptible to rapid ice mass loss (Shen et al., 2018). Elevated GHF in Wilkes Land could therefore enhance this instability by encouraging ice flow across the grounding line.

5.2 Comparing predictions of geothermal heat flow

Our estimates of GHF exhibit similar spatial structure to that estimated by Shen et al. (2020), albeit with less short-wavelength variation. The study conducted by Shen et al. (2020) calibrated an empirical mapping between GHF and V_S using the observed relationship across the continental United States between interpolated heat flow measurements and V_S at 80 km depth from a regional tomographic model. When the US-calibrated mapping is applied to their Antarctic velocity model, resulting GHF ranges from 40 to 90 mW m^{-2}. Our results agree on the presence of anomalously high heat flow (approximately 80 mW m^{-2}) stretching from the Ross Sea to the Antarctic Peninsula, avoiding the coast between the Ross and Amundsen Sea. The most obvious discrepancy between the two structures is the presence of a high heat flow anomaly in our study, situated within the footprint of the Gamburtsev Mountain Range. The reliability of this particular prediction should be doubted, because while the geological origin of the Gamburtsev Mountains is not well known, the potential for it to be caused by a mantle plume would imply thin lithosphere in this region. This is not corroborated by our LAB depth model, or those of Richards et al. (2020b) or Priestley et al. (2018) (Figure 10a; b; d). We find that the spatial pattern of elevated GHF coincides with anomalously thick ($\sim$ 60 km) crust found in ANT-20. Since a constant radiogenic heat production is assumed throughout this crustal layer, thick crust steepens the geothermal temperature gradient and therefore increases the inferred GHF. We therefore hypothesise that the GHF anomaly arises from a combination of two factors. First, a discrepancy between the assumed and true crustal thickness in this region. Secondly, a discrepancy between the assumed and true radiogenic heat production.

5.3 Reconciling observations and predictions of mantle viscosity

Thermomechanical structure beneath the Amundsen Sea Embayment (ASE) is of particular pertinence, given the importance of this area as a potential indicator of West Antarctic ice sheet stability. While the ASE accounts for less than 4% the area of the AIS, the marine-grounded portion of the WAIS in this region accounts for a

quarter of the global present-day cryospheric contribution to GMSL rise (Barletta et al., 2018). The Pine Island and Thwaites glaciers are potentially vulnerable to catastrophic collapse, due to increasing ice flow rates, as well as a rapidly retreating and unstable grounding line (Barletta et al., 2018). The recent study of Barletta et al. (2018) provides a geodetic analysis of bedrock deformation rates across the ASE by the installation of six GPS stations. Observed GPS uplift rates were combined with an estimate of the local ice sheet history to estimate a Maxwell viscosity consistent with the applied constraints. Barletta et al. (2018) estimated a shallow upper mantle (SUM; base of lithosphere to 200 km) viscosity of $\eta_{\mathrm{SUM}}^{\mathrm{GPS}} = 10^{18-18.8}$ Pa s, and a deep upper mantle (DUM; 200 to 400 km) viscosity of $\eta_{\mathrm{DUM}}^{\mathrm{GPS}} = 10^{18.6-19.8}$ Pa s. These extremely low viscosities imply GIA response times of order 10 to 100 years, meaning that the topographic response to deglaciation following the Last Glacial Maximum (LGM; ~ 21 ka) would have already decayed away in this region. Since models of GIA in response to modern-day ice mass loss typically assume upper mantle viscosities of $\eta \sim 10^{20}$ Pa s, an upward revision of viscoelastic uplift rates would be required in the ASE, resulting in an upward revision of local ice mass loss of approximately 10%. Conversely, the vulnerability of the WAIS in this region to catastrophic collapse would potentially be reduced by the faster GIA response rates, due to the stabilising effect of rapid grounding line uplift as a glacier positioned on a reverse bed slope retreats.

To assess the implications of our inferred thermomechanical stucture for solid-Earth–ice-sheet interactions within the ASE, we used a polygon defined by the region $\theta = 240.0$ to $280.0°$, $\phi = -71.0$ to $-78.0°$ to approximate the spatial coverage of the area sensitive to local melting. Estimates of SUM and DUM viscosity were calculated by averaging the spatially variable viscosity, $\eta(\theta, \phi, z)$, for each anelasticity model within the set of $N_U = 1,000$ posterior samples. The resulting distribution of SUM and DUM viscosities were summarised according to equations (23) and (24), resulting in a mean and standard deviation, with the latter reflecting both spatial and physical uncertainty. We find values $\eta_{\mathrm{SUM}} = 10^{19.9\pm0.1}$ Pa s and $\eta_{\mathrm{DUM}} = 10^{20.0\pm0.3}$ Pa s. A similar approach was taken to estimate the regional LAB depth and GHF where, in the case of these two variables, spatial variance was purely lateral. This resulted in the values $z_{\mathrm{LAB}} = 60 \pm 10$ km and GHF $= 80 \pm 3$ mW m^{-2}.

Our viscosity estimates lie up to 2 orders of magnitude larger than that of Barletta et al. (2018), and are associated with LAB depths in keeping with the West Antarctic average $z_{\mathrm{LAB}} = 63 \pm 13$ km. However, our seismologically derived viscosities may in fact be in agreement with their geodetically derived counterparts, due to the timescale dependence of viscosity. The rheological response of a viscoelastic body to a given change in the stress field (i.e., forcing) depends on the time scale, τ, over which it occurs (Lau et al., 2019). Frequency-dependent anelasticity parameterisations can be used to calculate viscosity at any forcing time scale, and the values we report in this study are for steady state, representing the theoretical limit of an infinite forcing time scale. On the other hand, geodetically determined viscosities are relevant to the forcing time scale corresponding with the deformation process in operation. The shorter the forcing time scale, the larger the discrepancy between steady state and apparent viscosity, as the deformation behaviour tends towards elastic. Assuming τ in the range 10 to 100 years, we estimate a reduction in η_{SUM} of 0.5 to 1.4 orders of magnitude between steady state and the observed deformation time scales (Lau et al., 2021). In terms of η_{DUM}, the equivalent reduction is 0.6 to 1.5 orders of magnitude. In each case, this is significant enough to bring our results into close agreement with those of Barletta

et al. (2018), indicating that the thermomechanical predictions made in this study are consistent with geodetic observations. Our findings suggest that, if gravimetric data is corrected for the effect of recent melting using GIA models that assume steady state viscosities and do not account for frequency-dependent scaling, contemporary ice mass loss will be consistently underestimated. We note that the ability of the WAIS to stabilise itself via rapid bedrock uplift in response to local ice mass changes may also be increased by the forcing time scale dependence of mantle rheology.

5.4 Remaining Uncertainties

Despite making major progress in understanding the thermomechanical structure of the Antarctic upper mantle, our work highlights outstanding challenges that limit our ability to utilise seismological data to understand solid Earth structure and its relationship with cryospheric evolution. A lack of geophysical data sets containing information about the deep mantle restricts the precision with which we can estimate pressure-dependent behaviour. For example, the uncertainty present in our estimate of activation volume remains high after calibrating the anelasticity parameterisation, since the majority of our data relates to the shallowest 125 km of the mantle. This leads to increasing uncertainty in thermomechanical structure with depth. In addition, the microphysical process or processes responsible for the onset of anelasticity is subject to significant debate, and this translates into competing methods for modelling anelastic effects (Faul et al., 2007; Yamauchi et al., 2016). As a result, heavily discrepant predictions may be made depending on the choice of physical model (Ivins et al., 2021). With this in mind, our inverse calibration has been designed structurally to work with any choice of anelasticity parameterisation. Further uncertainty relates to the particular viscous creep mechanism dominating Antarctic upper mantle rheology on time scales relevant to the modelling of geodynamic processes (Lau et al., 2019). If dislocation creep is the dominant mechanism, the steady-state diffusion creep viscosities predicted here will be less useful. However, the temperatures we predict would remain robust (see Supporting Information for temperature structures), being reliant only on the correct modelling of anelasticity at seismic frequency.

With respect to secondary structures calculated using our estimates of three-dimensional temperature variations, namely LAB depth and geothermal heat flow, a few specific challenges are yet to be addressed. First, vertical seismic resolution limits make it difficult to infer LAB depth variations smaller than $\sim$ 15 km. Secondly, due largely to the downward bleeding of slow shear-wave velocities associated with discrepancies between the modelled and true crustal structure, seismically inferred temperature structure becomes unreliable close to the Moho. This means that interpolation must be used to estimate shallow temperature structure. While this is not expected to influence our estimates of LAB depth, since the 1200°C isotherm is sufficiently deep, it will have an effect on our estimates of heat flow, which are proportional to the surface geothermal gradient. A lack of exposed outcrops where Antarctic geothermal heat flow can be measured makes it difficult to ground truth our geophysical predictions and refine the model. In addition, we currently have a poor understanding of the range, depth variation, and lateral variation in Antarctic crustal heat production and conductivity. Since both of these parameters must be assumed to fit a steady-state geothermal profile to our temperature-depth data, our geothermal heat flow estimates are directly affected by this limitation. To address this, complementary geophysical methods should be used to gain insight

into crustal heat production and conductivity structure, allowing for further refinement of GHF models.

6 Conclusions

A probabilistic approach to the calibration of experimental parameterisations of anelasticity has been developed to provide a self-consistent mapping between three-dimensional seismic tomography data and models of thermomechanical structure. By making use of a physical model designed to account for frequency dependence in the mantle stress-strain relationship, it is possible to translate experimentally constrained microphysical behaviour into predictions of macroscopic variables including temperature, viscosity and density, as a function of shear-wave velocity. We calibrate the anelasticity parameters with a suite of regional geophysical data constraints, reducing the discrepancy in physical predictions offered by different seismic tomography models, and ensuring a set of outputs compatible with well-constrained mantle properties. We provide an implementation of the inverse theory, using the Globally Adaptive Scaling Within Adaptive Metropolis (GASWAM) adaptation of the Metropolis-Hastings algorithm to allow ideal sampling efficiency and thus make the inverse problem tractable. We have shown it is possible to utilise a small subset (in our case, 0.5%) of the overall posterior data set to propagate shear-wave velocity into accurate estimates of thermomechanical structure and its uncertainty, which ensures computational viability. By probing the model covariance structure, this uncertainty is significantly reduced as compared to treating parameters independently (viscosity uncertainty reduced by 4 to 5 orders of magnitude at 150 km depth).

Dramatic differences in viscosity structure, LAB depth and GHF are predicted between East and West Antarctica, in accordance with other studies (Barletta et al., 2018; Priestley et al., 2018; Richards et al., 2020b; Shen et al., 2020; Austermann et al., 2021). We find evidence for mostly thick lithosphere, high viscosity asthenosphere, and uniformly low GHF beneath the EAIS. Shallow LAB depths and high GHF coincide with regions characterised by the presence of low viscosity anomalies, such as in western Marie Byrd Land where $\eta = 10^{19.5\pm0.3}$ Pa s, $z_{\mathrm{LAB}} = 50 \pm 10$ km, and GHF $= 90 \pm 5$ mW m^{-2}. This combination of thermomechanical properties is consistent with the geological record of regional Plio-Pleistocene magmatism (Sarbas, 2008; Ball et al., 2021), and indicates that western Marie Byrd Land, along with the eastern Ross Embayment and Antarctic Peninsula, may be amongst the most dynamic in response to climate and ocean forcing. High GHF may significantly increase the flow of ice towards the continental perimeter, whereas the presence of low viscosities and thin lithosphere suggest much faster bedrock uplift rates than a one-dimensional average rheology, potentially providing a stabilising effect on the grounding line (Gomez et al., 2010).

The outputs presented in this study may be used to refine our understanding of ice sheet stability in Antarctica. Our models of density structure can be used to improve time-dependent models of convectively supported surface topography, enabling correction of palaeo sea level markers used to inform ice sheet history. Our self-consistently determined viscosity and LAB depth structures, that also constrain time-dependent rheological variations, can be applied to three-dimensional glacial isostatic adjustment studies, where uplift rates are intimately tied to rheological structure. These high-resolution estimates of thermomechanical structure will be useful in constraining bedrock uplift rate across the continent, in turn altering corrections needed to produce gravimetric and altimetric estimates

of present-day ice mass loss rates. Our seismically inferred maps of geothermal heat flow can be incorporated in new ice-sheet modelling studies, where basal sliding rates are highly sensitive to the amount of thermal energy provided from below. As a result, we suggest that our new methodology for estimating solid Earth inputs and their associated uncertainties may enable accurate probabilistic assessment of ice sheet stability scenarios and projections of future sea level rise.

Acknowledgments: JANH acknowledges support from the Natural Environment Research Council (grant NE/S007415/1). FDR acknowledges support from the Imperial College Research Fellowship Scheme. GGR acknowledges support from the Natural Environment Research Council (grant NE/T012501/1). Figures were prepared using Generic Mapping Tools software. Model outputs are provided in Supporting Information and in an OSF online repository (https://doi.org/10.17605/OSF.IO/F4NTR). Code is provided in a GitHub repository (https://github.com/JamesHazzard/BANCAL22). The authors declare no competing financial interests.

References

An, M. et al. (2015). "Temperature, lithosphere-asthenosphere boundary, and heat flux beneath the Antarctic Plate inferred from seismic velocities". *J. Geophys. Res. Solid Earth* 120.12.

Andrieu, C. and J. Thoms (2008). "A tutorial on adaptive MCMC". *Statistics and Computing* 18.4.

Austermann, J., M. J. Hoggard, K. Latychev, F. D. Richards, and J. X. Mitrovica (2021). "The effect of lateral variations in Earth structure on Last Interglacial sea level". *Geophysical Journal International* 227.3.

Austermann, J., J. X. Mitrovica, K. Latychev, and G. A. Milne (2013). "Barbados-based estimate of ice volume at Last Glacial Maximum affected by subducted plate". *Nature Geoscience* 6.7.

Austermann, J. et al. (2015). "The impact of dynamic topography change on Antarctic ice sheet stability during the mid-Pliocene warm period". *Geology* 43.10.

Ball, P. W., N. J. White, J. Maclennan, and S. N. Stephenson (2021). "Global influence of mantle temperature and plate thickness on intraplate volcanism". *Nature Communications* 12.1.

Bamber, J. L., R. M. Westaway, B. Marzeion, and B. Wouters (2018). "The land ice contribution to sea level during the satellite era". *Environmental Research Letters* 13.6.

Barletta, V. and A. Bordoni (2013). "Effect of different implementations of the same ice history in GIA modeling". *Journal of Geodynamics* 71.

Barletta, V. R. et al. (2018). "Observed rapid bedrock uplift in Amundsen Sea Embayment promotes ice-sheet stability". *Science* 360.6395.

Burgos, G. et al. (2014). "Oceanic lithosphere-asthenosphere boundary from surface wave dispersion data". *J. Geophys. Res. Solid Earth* 119.2.

Burton-Johnson, A., R. Dziadek, and C. Martin (2020). "Review article: Geothermal heat flow in Antarctica: current and future directions". *The Cryosphere* 14.11.

Cammarano, F., S. Goes, P. Vacher, and D. Giardini (2003). "Inferring upper-mantle temperatures from seismic velocities". *Physics of the Earth and Planetary Interiors* 138.3.

Caron, L. et al. (2018). "GIA Model Statistics for GRACE Hydrology, Cryosphere, and Ocean Science". *Geophysical Research Letters* 45.5.

Champac, V. and J. Garcia Gervacio (2018). *Timing Performance of Nanometer Digital Circuits Under Process Variations*. 1st ed. Springer International Publishing. 204 pp.

Cobden, L., S. Goes, F. Cammarano, and J. A. D. Connolly (2008). "Thermochemical interpretation of one-dimensional seismic reference models for the upper mantle: Evidence for bias due to heterogeneity". *Geophysical Journal International* 175.2.

Coulon, V. et al. (2021). "Contrasting Response of West and East Antarctic Ice Sheets to Glacial Isostatic Adjustment". *Journal of Geophysical Research: Earth Surface* 126.7.

Dalton, C. A., C. H. Langmuir, and A. Gale (2014). "Geophysical and Geochemical Evidence for Deep Temperature Variations Beneath Mid-Ocean Ridges". *Science* 344.6179.

Davies, D. R. et al. (2019). "Earth's multi-scale topographic response to global mantle flow". *Nature Geoscience* 12.10.

DeConto, R. M. and D. Pollard (2016). "Contribution of Antarctica to past and future sea-level rise". *Nature* 531.7596.

Eilon, Z., K. M. Fischer, and C. A. Dalton (2018). "An adaptive Bayesian inversion for upper-mantle structure using surface waves and scattered body waves". *Geophysical Journal International* 214.1.

Faul, U. H. and I. Jackson (2005). "The seismological signature of temperature and grain size variations in the upper mantle". *Earth and Planetary Science Letters* 234.1.

Faul, U. H., I. Jackson, and Y. X (2007). "Diffusion creep of dry, melt-free olivine". *J. Geophys. Res.* 112.B4.

Fretwell, P. et al. (2013). "Bedmap2: improved ice bed, surface and thickness datasets for Antarctica". *The Cryosphere* 7.1.

Fukuda, J. and K. M. Johnson (2010). "Mixed linear–non-linear inversion of crustal deformation data: Bayesian inference of model, weighting and regularization parameters". *Geophysical Journal International* 181.3.

Gallagher, K., K. Charvin, S. Nielsen, M. Sambridge, and J. Stephenson (2009). "Markov chain Monte Carlo (MCMC) sampling methods to determine optimal models, model resolution and model choice for Earth Science problems". *Marine and Petroleum Geology* 26.4.

Gelman, A., W. R. Gilks, and G. O. Roberts (1997). "Weak convergence and optimal scaling of random walk Metropolis algorithms". *The Annals of Applied Probability* 7.1.

Gomez, N., K. Latychev, and D. Pollard (2018). "A Coupled Ice Sheet–Sea Level Model Incorporating 3D Earth Structure: Variations in Antarctica during the Last Deglacial Retreat". *Journal of Climate* 31.10.

Gomez, N., J. X. Mitrovica, P. Huybers, and P. U. Clark (2010). "Sea level as a stabilizing factor for marine-ice-sheet grounding lines". *Nature Geoscience* 3.12.

Haario, H., E. Saksman, and J. Tamminen (2001). "An Adaptive Metropolis Algorithm". *Bernoulli* 7.2.

Hirth, G. and D. Kohlstedt (2004). "Rheology of the Upper Mantle and the Mantle Wedge: A View from the Experimentalists". In: *Inside the Subduction Factory*. American Geophysical Union (AGU), pp. 83–105.

Hoggard, M. J. et al. (2020). "Global distribution of sediment-hosted metals controlled by craton edge stability". *Nature Geoscience* 13.7.

Ivins, E. R., W. van der Wal, D. A. Wiens, A. J. Lloyd, and L. Caron (2021). "Antarctic upper mantle rheology". *Geological Society, London, Memoirs* 56.

Jain, C., J. Korenaga, and S.-i. Karato (2019). "Global Analysis of Experimental Data on the Rheology of Olivine Aggregates". *Journal of Geophysical Research: Solid Earth* 124.1.

Jennings, S., D. Hasterok, and J. Payne (2019). "A new compositionally based thermal conductivity model for plutonic rocks". *Geophysical Journal International* 219.2.

Karato, S. and H. Jung (1998). "Water, partial melting and the origin of the seismic low velocity and high attenuation zone in the upper mantle". *Earth and Planetary Science Letters* 157.3.

King, M. A. et al. (2012). "Lower satellite-gravimetry estimates of Antarctic sea-level contribution". *Nature* 491.7425.

Klöcking, M. et al. (2020). "A tale of two domes: Neogene to recent volcanism and dynamic uplift of northeast Brazil and southwest Africa". *Earth and Planetary Science Letters* 547.

Korenaga, T. and J. Korenaga (2016). "Evolution of young oceanic lithosphere and the meaning of seafloor subsidence rate". *Journal of Geophysical Research: Solid Earth* 121.9.

Lau, H. C. P. et al. (2021). "Frequency Dependent Mantle Viscoelasticity via the Complex Viscosity: Cases From Antarctica". *J Geophys Res Solid Earth* 126.11.

Lau, H. C. P. and B. K. Holtzman (2019). ""Measures of Dissipation in Viscoelastic Media" Extended: Toward Continuous Characterization Across Very Broad Geophysical Time Scales". *Geophysical Research Letters* 46.16.

Lau, H. C. P. et al. (2016). "Inferences of mantle viscosity based on ice age data sets: Radial structure". *Journal of Geophysical Research: Solid Earth* 121.10.

Lee, C. (2003). "Compositional variation of density and seismic velocities in natural peridotites at STP conditions: Implications for seismic imaging of compositional heterogeneities in the upper mantle". *Journal of Geophysical Research: Solid Earth* 108.B9.

Lloyd, A. J. et al. (2020). "Seismic Structure of the Antarctic Upper Mantle Imaged with Adjoint Tomography". *Journal of Geophysical Research: Solid Earth* 125.3.

Maccaferri, F., E. Rivalta, D. Keir, and V. Acocella (2014). "Off-rift volcanism in rift zones determined by crustal unloading". *Nature Geoscience* 7.4.

Magee, C. et al. (2016). "Lateral magma flow in mafic sill complexes". *Geosphere* 12.3.

McCarthy, C. and Y. Takei (2011). "Anelasticity and viscosity of partially molten rock analogue: Toward seismic detection of small quantities of melt". *Geophys. Res. Lett.* 38.18.

McKenzie, D., J. Jackson, and K. Priestley (2005). "Thermal structure of oceanic and continental lithosphere". *Earth and Planetary Science Letters* 233.3.

Metropolis, N., A. W. Rosenbluth, M. N. Rosenbluth, A. H. Teller, and E. Teller (1953). "Equation of State Calculations by Fast Computing Machines". *J. Chem. Phys.* 21.6.

Milne, G. A. et al. (2018). "The influence of lateral Earth structure on glacial isostatic adjustment in Greenland". *Geophysical Journal International* 214.2.

Mitrovica, J. et al. (2020). "Dynamic Topography and Ice Age Paleoclimate". *Annual Review of Earth and Planetary Sciences* 48.1.

Morlighem, M. et al. (2020). "Deep glacial troughs and stabilizing ridges unveiled beneath the margins of the Antarctic ice sheet". *Nature Geoscience* 13.2.

Noble, T. L. et al. (2020). "The Sensitivity of the Antarctic Ice Sheet to a Changing Climate: Past, Present, and Future". *Reviews of Geophysics* 58.4.

Priestley, K. and D. McKenzie (2006). "The thermal structure of the lithosphere from shear wave velocities". *Earth and Planetary Science Letters* 244.1.

— (2013). "The relationship between shear wave velocity, temperature, attenuation and viscosity in the shallow part of the mantle". *Earth and Planetary Science Letters* 381.

Priestley, K., D. McKenzie, and T. Ho (2018). "A Lithosphere–Asthenosphere Boundary—a Global Model Derived from Multimode Surface-Wave Tomography and Petrology". In: *Lithospheric Discontinuities*. American Geophysical Union (AGU). Chap. 6, pp. 111–123.

Richards, F. D., M. J. Hoggard, L. R. Cowton, and N. J. White (2018). "Reassessing the Thermal Structure of Oceanic Lithosphere With Revised Global Inventories of Basement Depths and Heat Flow Measurements". *Journal of Geophysical Research: Solid Earth* 123.10.

Richards, F., M. Hoggard, A. Crosby, S. Ghelichkhan, and N. White (2020a). "Structure and dynamics of the oceanic lithosphere-asthenosphere system". *Physics of the Earth and Planetary Interiors* 309.

Richards, F. D., M. J. Hoggard, N. White, and S. Ghelichkhan (2020b). "Quantifying the Relationship Between Short-Wavelength Dynamic Topography and Thermomechanical Structure of the Upper Mantle Using Calibrated Parameterization of Anelasticity". *Journal of Geophysical Research: Solid Earth* 125.9.

Roy, V. (2020). "Convergence Diagnostics for Markov Chain Monte Carlo". *Annual Review of Statistics and Its Application* 7.1.

Sarbas, B. (2008). "The GEOROC database as part of a growing geoinformatics network". *Geoinformatics 2008—data to knowledge*. USGS, pp. 42–43.

Seroussi, H., E. R. Ivins, D. A. Wiens, and J. Bondzio (2017). "Influence of a West Antarctic mantle plume on ice sheet basal conditions". *Journal of Geophysical Research: Solid Earth* 122.9.

Shen, Q. et al. (2018). "Recent high-resolution Antarctic ice velocity maps reveal increased mass loss in Wilkes Land, East Antarctica". *Scientific Reports* 8.1.

Shen, W., D. A. Wiens, A. J. Lloyd, and A. A. Nyblade (2020). "A Geothermal Heat Flux Map of Antarctica Empirically Constrained by Seismic Structure". *Geophysical Research Letters* 47.14.

Shepherd, A. et al. (2018). "Mass balance of the Antarctic Ice Sheet from 1992 to 2017". *Nature* 558.7709.

Shepherd, A. et al. (2020). "Mass balance of the Greenland Ice Sheet from 1992 to 2018". *Nature* 579.7798.

Slangen, A. B. A. et al. (2017). "A Review of Recent Updates of Sea-Level Projections at Global and Regional Scales". *Surveys in Geophysics* 38.1.

Steinberger, B., C. P. Conrad, A. Osei Tutu, and M. J. Hoggard (2019). "On the amplitude of dynamic topography at spherical harmonic degree two". *Tectonophysics* 760.

Stixrude, L. and C. Lithgow-Bertelloni (2011). "Thermodynamics of mantle minerals - II. Phase equilibria". *Geophysical Journal International* 184.3.

Takei, Y. (2017). "Effects of Partial Melting on Seismic Velocity and Attenuation: A New Insight from Experiments". *Annual Review of Earth and Planetary Sciences* 45.1.

Thomas, I. D. et al. (2011). "Widespread low rates of Antarctic glacial isostatic adjustment revealed by GPS observations". *Geophysical Research Letters* 38.22.

Whitehouse, P. L. (2018). "Glacial isostatic adjustment modelling: historical perspectives, recent advances, and future directions". *Earth Surface Dynamics* 6.2.

Yabe, K. and T. Hiraga (2020). "Grain-Boundary Diffusion Creep of Olivine: 2. Solidus Effects and Consequences for the Viscosity of the Oceanic Upper Mantle". *Journal of Geophysical Research: Solid Earth* 125.8.

Yamauchi, H. and Y. Takei (2016). "Polycrystal anelasticity at near-solidus temperatures". *Journal of Geophysical Research: Solid Earth* 121.11.

Zwally, H. J. and M. B. Giovinetto (2011). "Overview and Assessment of Antarctic Ice-Sheet Mass Balance Estimates: 1992-2009". *Surveys in Geophysics* 32.4.

Zwally, J. H., M. B. Giovinetto, M. A. Beckley, and J. L. Saba (2012). *Antarctic and Greenland Drainage Systems*. GSFC Cryospheric Sciences Laboratory.

Appendices

A Work Done and Complex Compliance

In the following analysis, we make use of a complex representation of stress, σ^*, and strain, ε^*. The real stress, σ, and strain, ε, that would be measured can be calculated by projecting their complex representations onto a constant axis of choice. Here, we take the imaginary projection where $\sigma = \Im(\sigma^*)$ and $\varepsilon = \Im(\varepsilon^*)$.

If we consider a single Fourier component of the stress applied to the linear viscoelastic body, this can be written as

$$\sigma(t) = \Im(\sigma_0 \exp(-i\omega t)) = -\sigma_0 \sin(\omega t). \tag{1}$$

The complex compliance, $J^*(\omega)$, provides us with the connection between applied stress and strain response

$$\varepsilon^*(t) = J^*(\omega)\sigma^*(t), \tag{2}$$

$$\implies \varepsilon(t) = \Im(\sigma_0(J_1 + iJ_2)\exp(-i\omega t)) \tag{3}$$

$$\implies \varepsilon(t) = -\sigma_0 J_1 \sin(\omega t) + \sigma_0 J_2 \cos(\omega t). \tag{4}$$

The work done during each oscillatory cycle of applied stress is given by the integral

$$W = \oint \sigma d\varepsilon = \int_0^{2\pi/\omega} \sigma \frac{d\varepsilon}{dt}\, \mathrm{d}t, \tag{5}$$

and thus takes the form

$$W = \int_0^{2\pi/\omega} -\sigma_0 \sin(\omega t)\, \frac{d}{dt}(-\sigma_0 J_1 \sin(\omega t) + \sigma_0 J_2 \cos(\omega t))\, \mathrm{d}t, \tag{6}$$

$$\implies W = \omega \sigma_0^2 \int_0^{2\pi/\omega} \left(J_1 \sin(\omega t)\cos(\omega t) + J_2 \sin(\omega t)\sin(\omega t)\right)\, \mathrm{d}t, \tag{7}$$

$$\implies W = \pi \sigma_0^2 \left(0 \cdot J_1 + 1 \cdot J_2\right) = \pi \sigma_0^2 J_2. \tag{8}$$

We can therefore see that the out-of-phase compliance term, J_2, is responsible for energy dissipation, while the in-phase compliance term, J_1, is responsible for energy storage.

An equivalent representation for equation (4) can be found using a double-angle trigonometric expansion as follows

$$\varepsilon(t) = -\varepsilon_0 \sin(\omega t + \phi), \tag{9}$$

$$\implies \varepsilon(t) = -\varepsilon_0 \cos(\phi)\sin(\omega t) - \varepsilon_0 \sin(\phi)\cos(\omega t). \tag{10}$$

By comparison with equation (4), we can establish some useful relations between the complex compliance terms and the phase of the strain response as follows.

$$J_1 = \cos(\phi)\varepsilon_0/\sigma_0; \tag{11}$$

$$J_2 = -\sin(\phi)\varepsilon_0/\sigma_0; \tag{12}$$

$$\tan(\phi) = -J_2/J_1. \tag{13}$$

This shows us that the superposition of the elastic and viscous response introduces a phase delay, ϕ, between stress and strain, and is controlled by the ratio between loss and storage terms of the complex compliance.

B Prior Estimation

In order to specify the Gaussian prior distribution, a suitable estimate of each parameter, μ_i, and its uncertainty, s_i, is required. The priors on the elastic sector of the parameter space, $\boldsymbol{\mathcal{X}}_{\text{elastic}} = \{\mu_0, \partial\mu/\partial T, \partial\mu/\partial P\}$, were calculated by sampling a range of thermochemical states, $\boldsymbol{S} = \{X, P, T\}$, where X is pyrolitic composition defined in terms of the proportion of harzburgite to basalt. A database containing the dependence of elastic shear modulus on $\boldsymbol{S}$ was utilised to build a prior picture of $\boldsymbol{\mathcal{X}}_{\text{elastic}}$. This database was constructed using the software Perple_X

according to the method laid out by Cobden et al. (2008), using the compilation of thermodynamic parameters of Stixrude et al. (2011). Activation energy (E_A), activation volume (V_A) and the solidus gradient ($\partial T_S/\partial z$) were estimated by summarising literature reported values (Hirth et al., 2004; Jain et al., 2019). Reference viscosity (η_0) was estimated using the following equation,

$$\eta_0 = \frac{d_0^p}{A} \exp\left(\frac{E_A + P_0 V_A}{R T_0}\right), \tag{14}$$

where the reference thermodynamic state $(P_0, T_0) = (1.5\ \text{GPa}, 1200\ ^\circ\text{C})$, $d_0 = 1$ mm is the reference grain size, p its exponent, and A a scaling coefficient. By sampling A, p, E_A and V_A over suitable ranges retrieved from the literature (Hirth et al., 2004; Jain et al., 2019), a summary of η_0 could be established.

C Adaptive Metropolis Algorithms

The Metropolis-Hastings algorithm relies on a proposal distribution in order to generate transitions between a current state, $\mathcal{X}$, and a proposal state, $\mathcal{Y}$. The precise form and magnitude of the proposal distribution is a key component of the number of trials required to achieve ergodicity: the convergence of our discrete set of samples onto the underlying continuous posterior distribution.

Adaptive Metropolis algorithms are intended to improve the efficiency of this sampling process. Haario et al. (2001) serves as a good reference point for the implementation of such an algorithm. It utilises the condition found by Gelman et al. (1997) that for a Metropolis algorithm on $\mathbb{R}^d$, the proposal is optimally scaled when the proposal state is generated according to

$$\boldsymbol{\mathcal{Y}}^{n+1} \sim \mathcal{N}\left(\boldsymbol{\mathcal{X}}^n, \boldsymbol{\Sigma}^{\text{proposal}}\right), \tag{15}$$

$$\boldsymbol{\Sigma}^{\text{proposal}} = \gamma \boldsymbol{\Sigma}^{\boldsymbol{\mathcal{X}}}, \tag{16}$$

where $\boldsymbol{\Sigma}^{\boldsymbol{\mathcal{X}}}$ is the posterior covariance matrix, and $\gamma = \frac{2.38^2}{d}$ is the scaling coefficient. The condition implies that the ideal proposal covariance matrix is a scalar multiple of the target posterior covariance. Since the posterior is the object we are attempting to access via our sampling procedure, employing a suitable proposal is challenging. To address this issue, Haario et al. (2001) use an unbiased estimate of the target posterior covariance, which can be calculated empirically based on the evolving chain of generated samples. On the n^{th} trial, where $n-1$ samples have been generated so far, the unbiased estimate of the posterior covariance is

$$\overline{\boldsymbol{\Sigma}}^{\boldsymbol{\mathcal{X}}} = \frac{1}{n-2} \sum_{i=1}^{n-1} \left(\boldsymbol{\mathcal{X}}^i - \overline{\boldsymbol{\mathcal{X}}}\right) \left(\boldsymbol{\mathcal{X}}^i - \overline{\boldsymbol{\mathcal{X}}}\right)^T, \tag{17}$$

where $\overline{\boldsymbol{\mathcal{X}}} = \frac{1}{n-1} \sum_{i=1}^{n-1} \mathcal{X}_i$. The prefix "adaptive" therefore comes from the iterative adaptation of the proposal covariance matrix. For multi-dimensional parameter spaces ($d > 1$), $\overline{\boldsymbol{\Sigma}}^{\boldsymbol{\mathcal{X}}}$ may take a considerable number of trials to resemble the true posterior covariance, $\boldsymbol{\Sigma}^{\boldsymbol{\mathcal{X}}}$, however, it should provide better performance than a fixed proposal setup. Substituting $\boldsymbol{\mathcal{X}}$ in equation (17) for only the subset of trial models that were accepted, $\boldsymbol{\mathcal{Z}}$, may offer more

efficient convergence towards the posterior covariance. This approach is known as the "greedy start" procedure, and we make use of it in this study (Figure 3). It should also be noted that since equation (17) relies on the history of all preceding trials, the chain of samples is no longer Markovian. However, it has been proven that ergodicity still holds for adaptive algorithms given some loose assumptions on the posterior (see Haario et al., 2001 for details).

Implementation of the Adaptive Metropolis algorithm shown above is theoretically easy, however the optimal scaling factor, $\gamma = \frac{2.38^3}{d}$, does not work in practice if there are significant correlations between the parameters in the model. In this case, the solution is to also update γ adaptively. The Global Adaptive Scaling Within Adaptive Metropolis (GASWAM) scheme employs this technique to estimate a suitable proposal covariance matrix

$$\mathbf{\Sigma}^{\text{proposal}} = \gamma^n \left(\overline{\mathbf{\Sigma}}^{\boldsymbol{\mathcal{X}}} + \epsilon \mathbf{1} \right), \tag{18}$$

$$\gamma^n = \gamma^{n-1} + \eta^n (a^{n-1} - a^*). \tag{19}$$

Here, the scaling factor to be used for the n^{th} trial, γ^n, is updated by a factor proportional to the difference between the current and ideal acceptance ratios, a^{n-1} and a^*, respectively. The function, $\eta^n = n^{-1/2}$, is used to ensure adaptation decays in size as the simulation progresses. The presence of the constant $\epsilon > 0$ ensures ergodicity, and is chosen to be negligibly small compared to the size of the proposal covariance matrix. This algorithm can be employed after some fixed number of trials — long enough to provide a suitable first estimate of $\mathbf{\Sigma}^{\text{proposal}}$ — and initiated with the traditional Adaptive Metropolis scaling factor $\gamma^0 = 2.38^2/d$.

D Approximating the relationship between elastic shear-wave velocity and temperature

The linear region of the $V_S(T)$ relationship in a given depth bin is well-approximated by assuming an elastic response at fixed pressure. Consider the 50 to 75 km depth bin (Figure 4a, blue circles), and let us define a reference shear modulus relevant to this depth slice as follows

$$\mu_0^* = \mu_0 + \partial\mu/\partial P \, (P - P_0), \tag{20}$$

where $P = 2.1$ GPa is the corresponding pressure value. The $V_S(T)$ relationship can be expressed as

$$V_S(T) = \sqrt{\frac{\mu(T)}{\rho(T)}}, \tag{21}$$

and therefore, in terms of our renormalised shear modulus,

$$V_S(T) = \sqrt{\frac{\mu_0^* + \partial\mu/\partial T \, (T - T_0)}{\rho(T)}}. \tag{22}$$

Since density is only expected to vary by 2% over the temperature range covered by the 50 to 75 km depth bin of the plate V_S data, and even less so for the other two depth bins, we ignore its variation for the sake of simplicity here. Consider the numerator, $\zeta = \sqrt{\mu_0^* + \partial\mu/\partial T\,(T - T_0)}$, of equation (22). This may be rewritten in the form

$$\frac{\zeta}{\sqrt{\mu_0^*}} = \left(1 + \frac{\partial\mu/\partial T}{\mu_0^*}\Delta T\right)^{\frac{1}{2}}, \tag{23}$$

Assessing the magnitude of each term on the right hand side of this equation, $|\mu_0| \sim 10^2$ GPa and $\left|\partial\mu/\partial T\Delta T\right| \sim 10^1$ GPa, we find it is possible to perform a binomial expansion since the ratio

$$\left|\frac{\partial\mu/\partial T}{\mu_0^*}\Delta T\right| < 1. \tag{24}$$

Therefore, expanding the square-root, we have

$$\zeta = \sqrt{\mu_0}\left(1 + \frac{1}{2}\frac{\partial\mu/\partial T}{\mu_0}\Delta T + \mathcal{O}((\Delta T)^2)\right). \tag{25}$$

Ignoring terms of second-order and above, we can deduce the form of the linear relationship $\zeta(T)$ as follows

$$\zeta \approx \sqrt{\mu_0}\left(1 + \frac{1}{2}\frac{\partial\mu/\partial T}{\mu_0}\Delta T\right), \tag{26}$$

and thus in terms of shear-wave velocity we have

$$V_S(T) = \sqrt{\frac{\mu_0}{\rho}} + \frac{1}{2}\frac{\partial\mu/\partial T}{\mu_0\rho}\Delta T. \tag{27}$$